Journal of Medicinal Chemistry

pubs.acs.org/jmc

Article

Structure-Based Design of Bisubstrate Tetracycline Destructase Inhibitors That Block Flavin Redox Cycling

Emily E. Williford, Caitlin M. DeAngelo, Kevin S. Blake, Hirdesh Kumar, Kendrick K. Lam, Katherine V. Jones, Niraj H. Tolia,* Gautam Dantas,* and Timothy A. Wencewicz*

Cite This: *J. Med. Chem.* 2023, 66, 3917−3933

Read Online

ACCESS | Metrics & More | Article Recommendations | Supporting Information

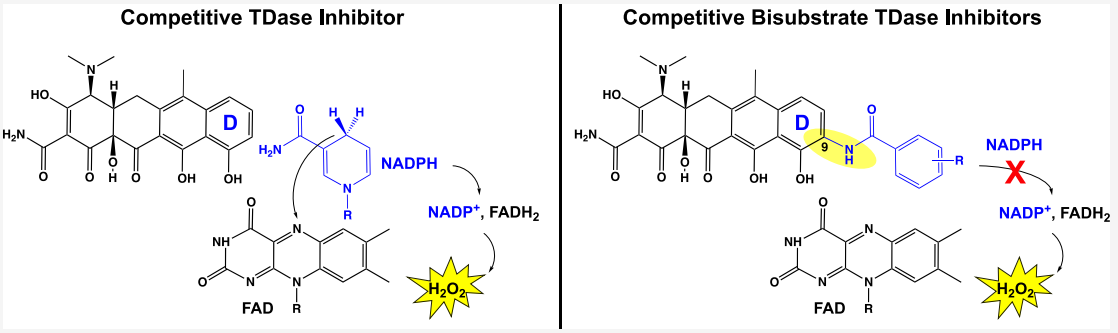

ABSTRACT: Tetracyclines (TCs) are an important class of antibiotics threatened by an emerging new resistance mechanism—enzymatic inactivation. These TC-inactivating enzymes, also known as tetracycline destructases (TDases), inactivate all known TC antibiotics, including drugs of last resort. Combination therapies consisting of a TDase inhibitor and a TC antibiotic represent an attractive strategy for overcoming this type of antibiotic resistance. Here, we report the structure-based design, synthesis, and evaluation of bifunctional TDase inhibitors derived from anhydrotetracycline (aTC). By appending a nicotinamide isostere to the C9 position of the aTC D-ring, we generated bisubstrate TDase inhibitors. The bisubstrate inhibitors have extended interactions with TDases by spanning both the TC and presumed NADPH binding pockets. This simultaneously blocks TC binding and the reduction of FAD by NADPH while "locking" TDases in an unproductive FAD "out" conformation.

INTRODUCTION

Tetracycline (TC) antibiotics are a family of type-II polyketides originally isolated from *Streptomyces aureofaciens*.[1] TCs have been in clinical use for >70 years as broad-spectrum antibiotics and continue to be used as frontline agents for treating a variety of infections caused by Gram-positive and Gram-negative bacteria.[2−4] Until recently, it was thought that clinical TC resistance occurred primarily through the expression of efflux pumps and ribosome protection proteins.[5] These resistance mechanisms have been largely overcome in the clinic by the development of last-generation TCs known as the glycylcyclines, including the FDA-approved drugs tigecycline, eravacycline, and omadacycline.[6−8] Unfortunately, all known TC antibiotics are susceptible to an emerging third route of clinical resistance: enzymatic inactivation by tetracycline destructase (TDase) enzymes.[9,10]

TDases are members of the class A flavin monooxygenase (FMO) enzyme family.[11] TDases are FAD-dependent and use an NADPH/O_2-coupled redox cycle to catalyze the inactivation of TC antibiotics.[11−13] Oxidation of the bound TC substrate occurs via a C4a-peroxy-flavin intermediate, resulting in substrate-dependent oxygen transfer (hydroxylation) and oxygen insertion (Baeyer−Villiger type) reactions (Figure 1A).[11,12,14] The resulting oxidized TC scaffolds lack antibacterial activity, presumably due to a loss of binding affinity for the bacterial ribosome.[15] TDases contain distinct substrate and FAD-binding domains connected via a C-terminal bridge helix (Figure 1B).[10,16−18] Two distinct types of TDases have <20% sequence homology and cluster by structural features, resistance phenotype, and ecological origin.[11] Type 1 TDases [represented in this study by Tet(X7)] have a constitutively open active site, provide resistance against all known TC antibiotic classes, and are found in human gut commensals and pathogens. Type 2 TDases [represented in this study by Tet(50)] contain an extra C-terminal helix that "gates" the active site during the catalytic cycle, provide resistance to only first- and second-generation TC antibiotics but not glycylcyclines, and are found primarily

Received: October 5, 2022
Published: March 6, 2023

https://doi.org/10.1021/acs.jmedchem.2c01629
J. Med. Chem. 2023, 66, 3917−3933

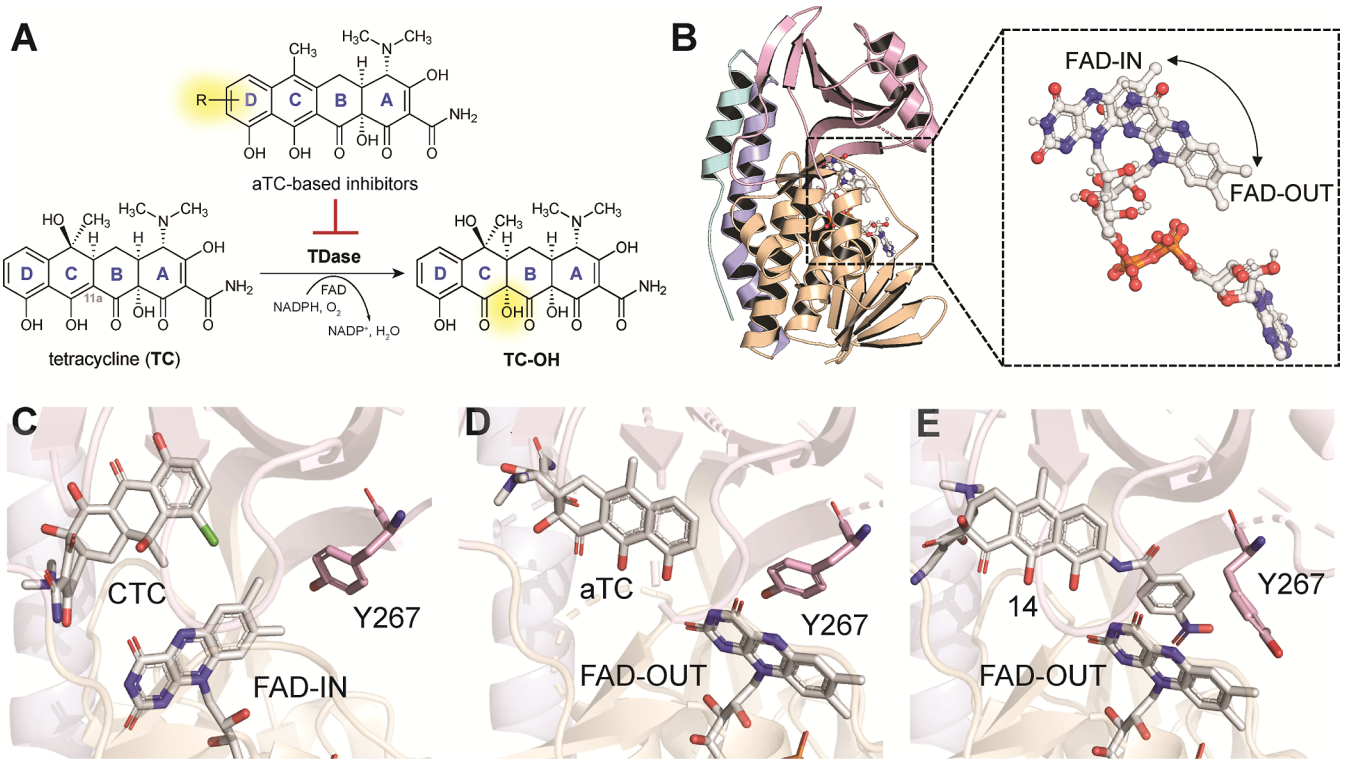

Figure 1. Structure-based design of C9-aTC derivatives as mechanism-based TDase inhibitors. (A) TDase-catalyzed hydroxylation of TC at C11a to generate inactive TC-OH to achieve TC-resistance. (B) Structure of Tet(50) with overlay of FAD-IN (chain A, PDB 5TUE) and FAD-OUT conformations (chain B, PDB 5TUE). (C) Structure of Tet(50) bound to CTC with FAD-IN (PDB 5TUI). (D) Structure of Tet(50) bound to aTC with FAD-OUT stabilized by Y267 (chain B, PDB 5TUF). (E) Structure of compound **14** docked into the Tet(50) active site with FAD-OUT stabilized by the C9-benzamido substituent displacing Y267 rotated toward solvent. Docking performed using Glide and structures visualized using PyMOL v2.3.2.

in environmental microbes. The structural and functional differences of type 1 and type 2 TDases have an important influence on substrate binding mode, flavin dynamics, mechanism of TC inactivation, and inhibition. At this point, type 1 TDases appear to be the more likely clinical threat, but the evolutionary connection between type 1 and type 2 TDases presents a unique opportunity to study TC resistance via enzymatic inactivation.

Enzymatic antibiotic inactivation is of particular concern given that this pathogen phenotype depletes the antibiotic challenge for the entire infection environment (including cells not expressing inactivating enzymes).[19] Evolution of antibiotic inactivation enzymes under intense selective pressure is a potential gateway to pan resistance against entire drug classes.[20] The clinical significance and global impact of this resistance mechanism have been fully realized for β-lactam antibiotics, where widespread dissemination of β-lactamase encoding genes demands the co-administration of a β-lactamase inhibitor to restore clinical efficacy of β-lactam antibiotics.[21,22] Presumably, TDase inhibitors will be needed in the future given the mobilization and widespread distribution of TDase genes in the environment, including clinical and agricultural settings.[23−25] The emergence of TDases in clinical pathogens is on an upward trajectory and the deployment of new glycylcyclines could exacerbate this trend as has been observed following the release of new broad-spectrum β-lactam antibiotics.[21] Anhydrotetracycline (aTC), which differs from parent TC by dehydration of the C6 alcohol, is a pan-TDase inhibitor and rescues whole cell activity of TC antibiotics in *Escherichia coli* and *Mycobacterium abscessus*.[16,26] The co-crystal structure of aTC bound to the type 2 TDase Tet(50) reveals a binding mode that is unique from the observed substrate binding mode leading to stabilization of the FAD-cofactor in an unproductive "OUT" conformation that is stabilized through a $\pi-\pi$ stacking interaction with the benzylic sidechain of Y267 (Figure 1C,D).

In addition to the TDase inhibitory activity, aTC alone has inherent antibacterial activity and some general toxicity at the effective concentrations (low μM) due in part to its ability to disrupt cellular membranes.[27,28] Further, some type 1 TDases can turnover aTC as a slow substrate indicating that aTC can sample the productive substrate binding mode with FAD in the "IN" conformation.[11,16,29] Simple modifications of the aTC scaffold, including halogenation of C7 and C9 of the D-ring or demethylation of C6 of the C-ring, were tolerated but failed to mitigate these potential liabilities.[29] Thus, we were motivated in this work to rationally design more effective TDase inhibitors with improved selectivity, potency, and stability by using structure-guided molecular modeling (Figure 1E). We identified a solvent-exposed channel between the aTC D-ring and Y267 in the aTC-Tet(50) co-crystal structure (PDB: 5TUF) that appeared to be accessible by benzamide and benzylamine substituents appended to the C9-position of the aTC D-ring. Hence, we designed and synthesized a series of "bisubstrate" TDase inhibitors predicted to span the aTC binding site and occupy the space filled by Y267 used to stabilize FAD in the "OUT" conformation through $\pi-\pi$ stacking of the aryl substituent with the FAD isoalloxazine heterocycle. This is also the space proposed to be occupied by the NADPH nicotinamide ring during FAD reduction. The

https://doi.org/10.1021/acs.jmedchem.2c01629
J. Med. Chem. 2023, 66, 3917−3933

Scheme 1. Synthesis of C9-aTC Derivatives (2−21)

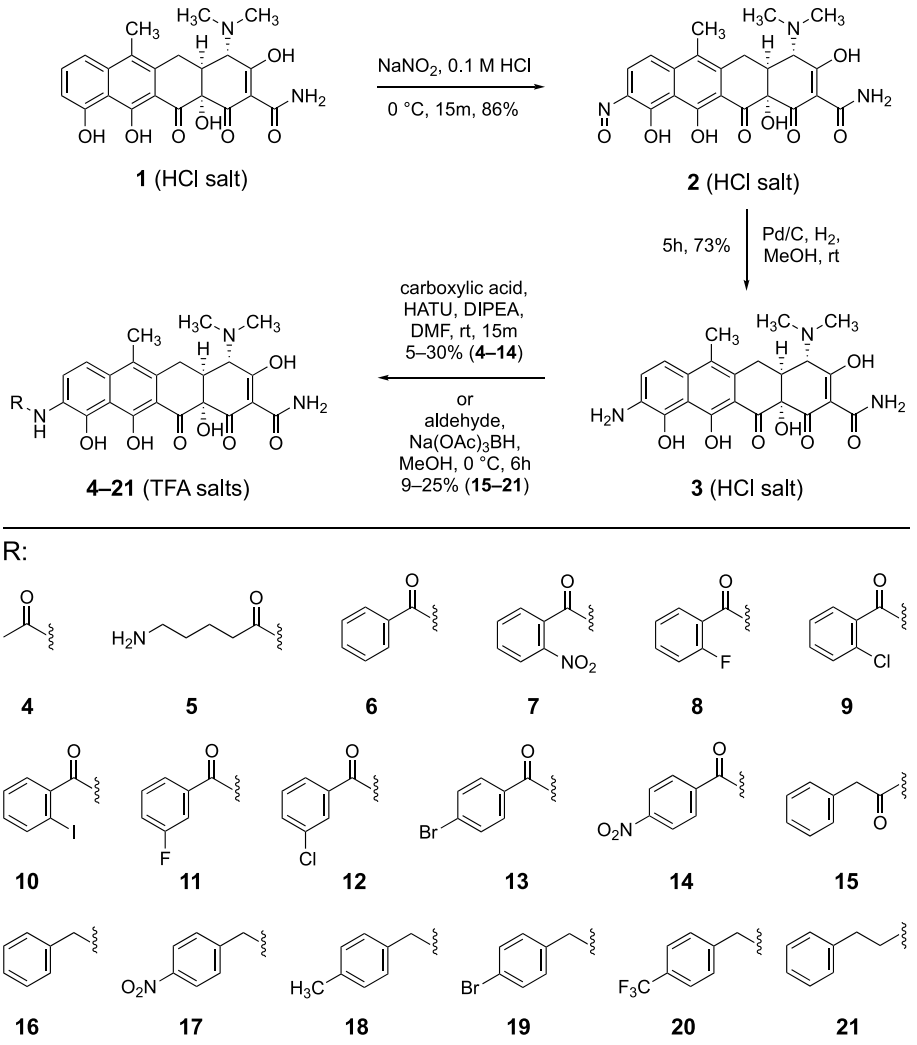

rationally designed bisubstrate inhibitors were stable toward TDase-catalyzed oxidation, eliminating the slow catalytic turnover observed for aTC and showed dose-dependent recovery of TC activity in whole cell assays. We report informative structure−activity relationships (SAR) and mechanistic studies to guide future inhibitor optimization and identify synergistic inhibitor−antibiotic pairs to overcome TC resistance via enzymatic inactivation. Our approach to bisubstrate mechanism-based inhibitor design exploits flavin dynamics, perturbs redox couples, and may be broadly applicable across the class A FMO enzyme family.

RESULTS AND DISCUSSION

Structure-Based Design of Bisubstrate TDase Inhibitors. The structure of the aTC-Tet(50) inhibition complex (PDB: 5TUF) shows aTC bound in the active site adjacent to and overlapping with the substrate binding site. The A-ring of aTC points toward the entrance of the active site, and the D-ring extends toward a solvent-exposed channel.[16] The FAD cofactor is trapped in the "OUT" conformation and is sterically occluded from accessing the "IN" conformation by the bound aTC inhibitor. The FAD "OUT" conformation is stabilized through a hydrogen bond between the flavin N3−H and the aTC C10−OH and a $\pi-\pi$ stacking interaction with the 4-hydroxy-benzyl sidechain of Y267[16] (Figure 1D). A similar Tyr-mediated $\pi-\pi$ stacking interaction has been observed for other FMOs, including kynurenine-3-monooxygenase (KMO).[30−34] A group at GlaxoSmithKline (GSK) proposed that this Tyr residue occupies the space that must be filled by the nicotinamide portion of NADPH during the reductive step.[35] No co-crystal structure of a class A FMO liganded with NAD(P)H or NAD(P)$^+$ in a catalytically relevant conformation has been reported, and the functional binding site for this cosubstrate remains elusive.[33,36] The GSK group used X-ray structures of KMO with competitive inhibitors occupying the substrate binding site combined with molecular docking of NADP$^+$ to guide the design of bisubstrate inhibitors composed of known benzoxazolidinone inhibitor scaffolds fused with nicotinamide isosteres.[35] We adapted the GSK scaffold hybridization approach to design a series of benzamide and benzylamine-substituted aTC analogues as potential bisubstrate inhibitors of TDases.

We used the co-crystal structure of aTC in complex with the type 2 TDase Tet(50) (PDB: 5TUF) as a template for molecular modeling of bisubstrate inhibitors (Figure 1D). We considered a variety of substituents at C9 of the bound aTC, which is ∼4.8 Å from the nearest carbon atom of the Y267 phenyl ring (compounds **1**−**21**; Scheme 1). We hypothesized that positioning an aryl substitution from the aTC D-ring at the C9-position could mimic the FAD isoalloxazine-Y267 $\pi-\pi$

https://doi.org/10.1021/acs.jmedchem.2c01629
J. Med. Chem. 2023, 66, 3917−3933

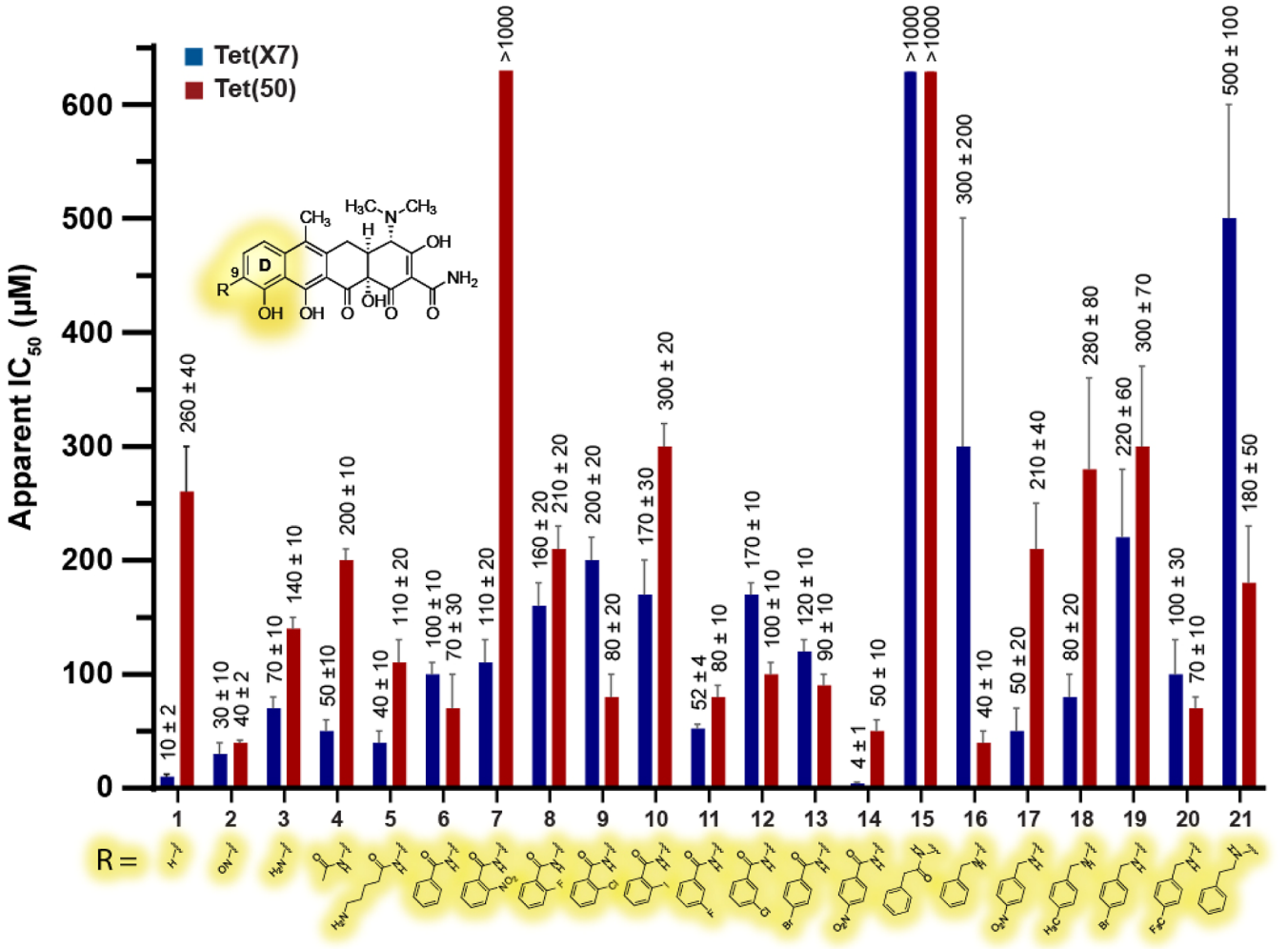

Figure 2. Apparent IC_{50} values measured through in vitro inhibition of Tet(X7) (blue) and Tet(50) (red) by compounds **1**–**21**. Error bars depict standard deviations for three independent trials.

stacking interaction and potentially improve inhibitor binding relative to the parent aTC scaffold. We used the Schrodinger platform to prepare the Tet(50) receptor using an alternate rotamer of Y267 allowing for the accommodation of C9-substituents (Figure S1A).[37] Molecular docking was performed using Glide and validated through the docking of aTC, which overlapped in good agreement with the experimentally observed binding mode (docking score = −7.1 kcal/mol; Figure S1B). We predicted the binding modes for *p*-NO_2-benzamide-C9-aTC (**14**) (docking score = −8.69 kcal/mol) and *p*-CF_3-benzylamine-C9-aTC (**20**) (docking score = −9.89 kcal/mol) analogues. The docked structures aligned well with the crystallographically observed aTC binding conformation and adopted an apparent $\pi-\pi$ stacking interaction with the FAD isoalloxazine ring. C9 of aTC is ∼3.8 Å and ∼5.0 Å from C1 and C2 of the phenyl substituents, respectively. These distances are in good agreement with the experimentally observed distance of ∼4.87 Å between C9 of aTC and the Y267 phenyl ring (Figures 1E and S1C,D). The top binding poses support the bisubstrate inhibitor design where amide and amine linked C9 aryl substituents on the aTC scaffold have the proper geometry needed to span the solvent accessible channel without disturbing the aTC inhibitor binding mode.

Synthesis of Bisubstrate TDase Inhibitors. We designed a simple and scalable semi-synthetic route to prepare aTC analogues via a C-9 amination strategy (Scheme 1). Initial attempts to nitrate aTC (**1**) under standard nitration conditions (HNO_3/H_2SO_4) produced mixtures of C-9 and C-7 nitro-aTC analogues. To our surprise, we serendipitously discovered that nitrosylation of aTC (**1**) proceeded smoothly with high regioselectivity for C-9 substitution. Treatment of aTC (**1**) with sodium nitrite under acidic conditions provided C9-nitroso-aTC (**2**) as the corresponding HCl salt in 86% yield. This stable nitroso compound was converted to the corresponding C9-amino-aTC (**3**) via Pd-catalyzed hydrogenolysis, resulting in 73% yield of the desired product. This simple two-step procedure can be accomplished on a gram scale to provide C9-amino-aTC (**3**) as the corresponding HCl salt with no chromatographic steps. We used C9-amino-aTC (**3**) as a central intermediate to access C9-aTC analogues with an amide or amine linkage via nucleophilic acyl substitutions with carboxylic acid substrates or reductive aminations with aldehyde substrates, respectively. Treatment of C9-amino-aTC (**3**) with various carboxylic acids under optimized amide coupling conditions (HATU, DIPEA, DMF, rt, 15 min) provided amides **4**–**15** as the corresponding TFA salts in 5–30% yield after final purification by prep-HPLC. Treatment of C9-amino-aTC (**3**) with various aldehydes under optimized reductive amination conditions ($Na(OAc)_3BH$, MeOH, 0 °C, 6 h) provided amines **16**–**21** as the corresponding TFA salts in

https://doi.org/10.1021/acs.jmedchem.2c01629
J. Med. Chem. 2023, 66, 3917−3933

9−25% yield after final purification by prep-HPLC. All compounds were fully characterized by NMR and HRMS, with purity analysis by LC−MS conducted prior to biological testing. Some samples contained varying amounts of C4-epimers as reported in the Methods section. Equilibration of C4-epimers is common for TC, aTC, and related compounds and is pH dependent.[38] C4-*epi*-TC has a reduced affinity for the ribosome and Tet repressor proteins, presumably due to the disruption of essential interactions between the A-ring substituents and conserved binding site residues.[16,39] We demonstrated that C4-*epi*-TC also has a reduced apparent binding affinity to Tet(X7) and Tet(50), and C4-*epi*-aTC is neither an inhibitor nor a substrate of these two enzymes (Figures S2−S6). Hence, we assumed that only the C4-(*S*) epimers of compounds **1**−**21** contributed significantly to the observed biological activities.

In Vitro SAR of Bifunctional TDase Inhibitors. We determined apparent IC_{50} values for compounds **1**−**21** against the type 1 TDase Tet(X7) and the type 2 TDase Tet(50) under steady-state conditions using TC as the substrate and NADPH as a cosubstrate. Reactions were initiated by the addition of TDase, without pre-incubation with inhibitors, and were monitored by the continuous measurement of optical absorbance at ∼400 nm (λ_{TC} monitoring for direct TC consumption) to determine linear velocities for each reaction. Apparent IC_{50} values were determined by plotting the observed reaction velocity versus log[inhibitor] and are visualized as bar graphs in Figure 2 for the convenient comparison of SAR for each enzyme type (Figures S7 and S8). We observed inhibition of Tet(X7) for 20 inhibitors (95% hit rate), with apparent IC_{50} values ranging from 3 to 600 μM adjusted for standard deviations. Similarly, 19 of the inhibitors were active against Tet(50) (90% hit rate) with a statistically significant range of apparent IC_{50} values from 38 to 370 μM.

Some notable SAR patterns emerged from the apparent IC_{50} values determined from the in vitro TDase inhibition assays (Figure 2). aTC (**1**) represents the parent inhibitor structure and provides a convenient reference point for comparing inhibitor potencies. The apparent IC_{50} values of aTC were 10 ± 2 and 260 ± 40 μM against Tet(X7) and Tet(50), respectively. These values are in good agreement with a previous report from our group [3 ± 1 and 210 ± 25 μM against Tet(X7) and Tet(50), respectively].[29] The reason for preferential inhibition of type 1 [Tet(X7)] over type 2 [Tet(50)] TDases by aTC (**1**) was not immediately clear, but we note that simple C9 substitutions including nitroso (**2**) and amino (**3**) groups reduced the inhibition of Tet(X7) (30 ± 10 and 70 ± 10 μM, respectively) and improved the inhibition of Tet(50) (40 ± 2 and 140 ± 10 μM, respectively) compared to the parent aTC scaffold. Amido substituents at C9 were generally well tolerated, with the simplest C9-acetamido (**4**) showing preference for inhibiting Tet(X7) (50 ± 10 μM) over Tet(50) (200 ± 10 μM). The bulkier C9-5-aminopentamide derivative (**5**) was also well tolerated, with apparent IC_{50} values of 40 ± 10 μM [Tet(X7)] and 110 ± 20 μM [Tet(50)].

The C9-benzamides **6**−**14** revealed a preference for *meta*- and *para*-substitution over *ortho*-substitution for both TDase types. Unsubstituted C9-benzamide **6** establishes a baseline for this series with apparent IC_{50} values of 100 ± 10 μM [Tet(X7)] and 70 ± 30 μM [Tet(50)], which are reduced inhibitory activities against Tet(X7) and enhanced inhibitory activity against Tet(50) compared to the parent aTC scaffold. Substitution of the phenyl ring with an *ortho*-NO_2 group (**7**) was well tolerated for Tet(X7) (110 ± 20 μM) but abolished inhibitory activity against Tet(50) (>1000 μM). Halogens in the *ortho*-position of C9-benzamides were better tolerated than *ortho*-nitration with a relatively tight range of apparent IC_{50} values of 140−220 μM [Tet(X7)] and 100−320 μM [Tet(50)] for *ortho*-F (**8**), *ortho*-Cl (**9**), and *ortho*-I (**10**). There is a slight preference for *meta*- and *para*-halogenation of C9-benzamides with apparent IC_{50} values ranging from 48 to 180 μM [Tet(X7)] and 70−110 μM [Tet(50)] for *meta*-F (**11**), *meta*-Cl (**12**), and *para*-Br (**13**). The *para*-NO_2 C9-benzamide **14** produced the lowest apparent IC_{50} value from the set against Tet(X7) (4 ± 1 μM) and showed a striking increase in activity against Tet(50) (50 ± 10 μM) compared to the *ortho*-NO_2 derivative (>1000 μM). Simple homologation from C9-benzamide to C9-phenylacetamide (**15**) abolished all TDase inhibitory activity, which deterred us from further pursuing phenyl substituted analogues in this series.

We next explored a series of C9-benzylamine derivatives (**16**−**20**) designed to maintain the same spacing as C9-benzamides between the C9-position of the aTC scaffold to the phenyl substituent (Figure 2). The C9-benzylamines allowed us to evaluate a more flexible C9-linkage relative to the rigid amide linkage in the C9-benzamide inhibitor series. We only investigated *para*-substitutions on the phenyl ring for the C9-benzylamine derivatives given the observed preference for this position in the benzamide series. Overall, inhibitor potency in the benzylamine series (apparent IC_{50} values ranging 30−500 μM) was in line with that observed for the benzamide series with a slight preference for inhibiting Tet(X7) over Tet(50) (except for compound **16**). Electron-withdrawing groups (NO_2, CF_3) on the phenyl ring of the benzylamine analogues were favored over donating groups (Me, Br) against Tet(X7), while the unsubstituted phenyl ring (**16**) was best against Tet(50). A homologated C9-phenethylamine derivative (**21**) showed moderate activity against Tet(50) (180 ± 50 μM) and diminished activity against Tet(X7) (500 ± 100 μM), similar to the homologated C9-phenylacetamide analogue **15**. The *para*-CF_3 analogue **20** was the most effective broad-spectrum inhibitor of type 1 and type 2 TDases in the benzylamine series, with apparent IC_{50} values of 100 ± 30 and 70 ± 10 μM against Tet(X7) and Tet(50), respectively.

To validate that the compounds can inhibit degradation of more clinically relevant substrates, we investigated the ability of aTC (**1**) and compound **14** to inhibit Tet(X7) degradation of tigecycline, a third-generation glycylcycline. Compounds **1** and **14** inhibited tigecycline degradation with apparent IC_{50} values of 1.2 ± 0.2 and 30 ± 11 μM, respectively (Figure S9). Independent biophysical validation of inhibitor binding was carried out using bio-layer interferometry (BLI). Treatment of TDases with EZ-Link NHS-PEG4-Biotin (Thermo Fisher) resulted in biotinylation of 7.4 mol biotin/mol Tet(X7) (22 Lys residues) and 6.1 mol biotin/mol Tet(50) (23 Lys residues). We compared Tet(X7) and Tet(50) binding of TC, **1**, and **14** (Figure S10) using BLI with super streptavidin tips (Sartorius). While we were unable to quantitatively fit the kinetic binding data, the qualitative binding curves consistently show that inhibitor **14** displays slower binding kinetics (k_{on} and k_{off}) compared to aTC, which is consistent with a bisubstrate mode of inhibition.

Rescue of TC Antibacterial Activity with Bisubstrate TDase Inhibitors. We selected a subset of C9-amide (compounds **4** and **14**) and C9-amine inhibitors (compounds

https://doi.org/10.1021/acs.jmedchem.2c01629
J. Med. Chem. 2023, 66, 3917−3933

16−20) for direct comparison with the parent inhibitor aTC (1) in the ability of TDase inhibitors to recover the antibacterial activity of TC in whole-cell bacterial growth experiments (Figure 3). We selected more compounds from

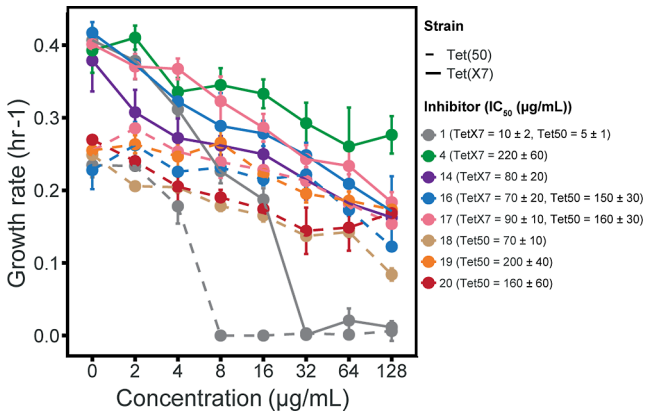

Figure 3. Dose-dependent recovery of TC activity by aTC (1) and C9-aTC derivatives (4, 14, 16−20) against *E. coli* MegaX expressing Tet(X7) (solid lines) or Tet(50) (dashed lines) from a pZE21 inducible vector. The *x*-axis represents the concentration of inhibitor (0−128 μg/mL) in the presence of constant TC (16 μg/mL). The *y*-axis represents growth rate generated from growth curve analysis, as described in the Methods section. The legend includes apparent IC_{50} values in μg/mL calculated for these data plots. Error bars represent the standard deviation for three technical replicates.

the amine series due to the similarity in apparent IC_{50} values from the in vitro TDase inhibition assays and the improved water solubility of these compounds compared to the amides. We used *E. coli* MegaX harboring pZE21 plasmid constructs for constitutive expression of Tet(X7) and Tet(50). Our group previously reported and validated this bacterial system for antibiotic susceptibility testing with TDase inhibitors and TC antibiotic combinations.[10,11,16] An important consideration for the interpretation of antibacterial combinations is the inherent antibacterial activity of each compound alone. The MIC values for TC against *E. coli* MegaX harboring pZE21-Tet(X7) and pZE21-Tet(50) were recorded as 512 and 128 μg/mL, respectively, using the standard broth microdilution method in MHII medium.[11,16] The MIC values for aTC (1) against the same strains were recorded as 64 μg/mL [Tet(X7)] and 16 μg/mL [Tet(50)].[16] In contrast, we found that compounds 4, 14, and 16−20 all lacked inherent antibacterial activity, with cell growth observed at concentrations up to 128 μg/mL.

We designed a combination study using TC antibiotic fixed at 16 μg/mL, severalfold lower than the recorded MIC values, with variable concentrations of TDase inhibitor (1, 4, 14, or 16−20) ranging from 0 to 128 μg/mL. We determined full bacterial growth curves during incubation at 37 °C with optical density at 600 nm measured over a 20 h window. The growth rate (reported as h^{-1}) was determined for each condition to compare the effects of TDase inhibitors in an unbiased manner (Figures 3 and S11). We observed dose-dependent rescue of TC activity by all the TDase inhibitors, with apparent IC_{50} values that agree with the in vitro potencies (Figure S12). The parent inhibitor aTC (1) appears to give the most potent rescue of TC activity with complete inhibition of bacterial growth observed at 32 and 8 μg/mL for Tet(X7)- and Tet(50)-producing strains, respectively, with apparent IC_{50} values of 10 ± 2 and 5 ± 1 μg/mL. For aTC, it is difficult to separate the contributions of TDase inhibition and inherent antibacterial activity at this concentration range. Hence, it is appreciated that while compounds 4, 14, and 16−20 fall short of providing complete growth inhibition at 16 μg/mL TC, there is a clear dose-dependent decrease in growth rates, consistent with TDase inhibition and TC rescue as the driver of this effect given these compounds independently possess no inherent growth inhibitory activity. All compounds tested resulted in significantly lower growth rates at concentrations ≥64 μg/mL, with significant decreases for compounds 14 and 18 with just 2 μg/mL (Figure S11). We confirmed these results on solid medium using the Kirby−Bauer agar diffusion antibacterial susceptibility assay for tigecycline against the Tet(X7)-expressing strain and for TC against the Tet(50)-producing strain (Figure S13). This modest yet promising bioactivity suggests that non-antibacterial TDase inhibitors can be developed to rescue TC antibiotic activity against bacterial pathogens expressing TC inactivating enzymes.

Bisubstrate TDase Inhibitors Block FAD Reduction by NADPH. Our prior biochemical characterization of aTC (1) inhibition of type 1 and type 2 TDases using Lineweaver−Burke analyses supports a model of competitive mechanism-based inhibition that is in agreement with the observed aTC binding mode in the Tet(50) co-crystal structure.[16,29] The new C9-substituted aTC analogues in this study were designed to be bisubstrate inhibitors that engage both the TC and NADPH binding sites. We hypothesized that a bisubstrate TDase inhibitor will competitively bind to both the TC and NADPH binding sites. To test this hypothesis, we used TC, aTC (1), and the *para*-NO_2-substituted C9-benzamide aTC analogue (14) to investigate the impact of TC antibiotics and TDase inhibitors on NADPH consumption. FMOs, including TDases, consume NADPH by reduction of FAD to $FADH_2$ that leads to the O_2-dependent formation of a reactive C4a-peroxy-flavin intermediate. FAD reduction by NADPH can be coupled to substrate oxidation or uncoupled, leading to the formation of H_2O_2. Detection of H_2O_2 has been used in diagnostic applications for TDase resistance in bacterial cultures.[40] Both the coupled and uncoupled pathways must be considered unless the substrate is omitted, where uncoupled H_2O_2 formation is the only viable path for enzyme turnover. Thus, H_2O_2 formation can serve as a proxy for FAD reduction by NADPH in FMOs.[41]

We analyzed TDase reactions with Tet(X7) and Tet(50) via optical absorbance (λ = 250−500 nm), LC−MS, and H_2O_2 formation (Figure 4 and Figure S14). We monitored the oxidation of Fe^{2+} to Fe^{3+} in the presence of xylenol orange to quantify H_2O_2 during TDase reactions. Xylenol orange provides a color change from orange to purple in the presence of H_2O_2 that can be monitored via optical absorbance at λ = 595 nm (Figure S14).[42] Both TC (Figure 4A) and aTC (Figure 4B) enhanced the rate of NADPH consumption for Tet(X7) and generated H_2O_2 in excess of the control (Figure 4G). LC−MS analysis of the reaction mixtures also showed that TC and aTC are oxidized by the addition of one ^{16}O to the scaffold, corresponding to the time and TDase-dependent formation of an observed $[M + O + H]^+$ molecular ion for each product. Conversely, the *para*-NO_2-C9-benzamide aTC analogue (14) reduced the rate of NADPH consumption, blocked H_2O_2 formation, and was stable over the 2 h duration of the reaction with Tet(X7) (Figure 4C). The results for TC with Tet(50) were similar to the Tet(X7) results where TC stimulated NADPH consumption, produced H_2O_2, and was

https://doi.org/10.1021/acs.jmedchem.2c01629
J. Med. Chem. 2023, 66, 3917−3933

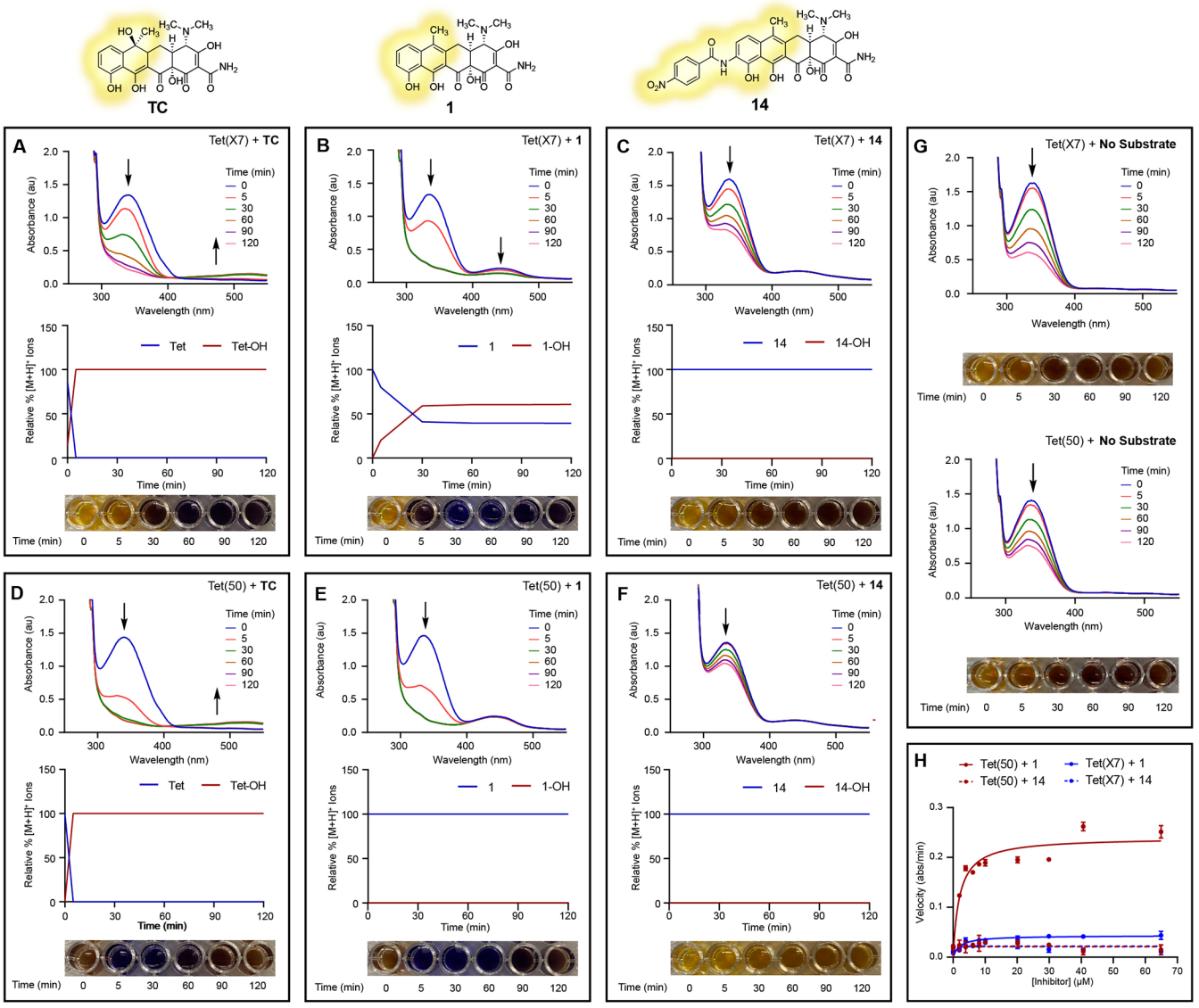

Figure 4. TC and aTC are substrates for TDases, while C9-aTCs are not TDase substrates. Panels (A–F) depict time-dependent optical absorbance, relative % LC–MS $[M + H]^+$ ion counts for substrates and products normalized to an internal standard, and H_2O_2 production for antibiotics (TC) and inhibitors (**1**, **14**) at 20 μM over the course of 0–120 min in the presence of TDases, Tet(X7), and Tet(50). Panel (G) depicts time-dependent optical absorbance for NADPH in the presence of Tet(X7) and Tet(50) with no TC substrate or inhibitor. Panel (H) depicts the apparent steady-state kinetics of NADPH consumption with increasing concentrations of aTC (**1**) and C9-aTC derivative **14**. All TDase reactions were performed in at least duplicate as independent trials using pure NADPH.

rapidly oxidized (Figure 4D). Like Tet(X7), aTC (**1**) stimulated NADPH consumption and produced H_2O_2 for the Tet(50) reaction. However, unlike the Tet(X7) reaction, aTC was stable over the reaction course with Tet(50) (Figure 4E). The result for the *para*-NO_2-C9-benzamide aTC analogue (**14**) against Tet(50) showed an even more pronounced reduction in the rate of NADPH consumption and H_2O_2 generation (Figure 4F).

We also analyzed apparent steady-state kinetics of NADPH consumption in the presence of variable TDase inhibitors, **1** or **14**, to determine K_{app} and v_{max} by fitting the observed reaction rates to the Michaelis–Menten equation (Figure 4H). In agreement with the results in Figure 4B,E, aTC (**1**) appeared to enhance the rate of NADPH consumption in a dose-dependent manner for Tet(X7) (K_{app} = 2.1 ± 0.3 μM, v_{max} = 0.043 ± 0.002 min^{-1}) and Tet(50) (K_{app} = 2.0 ± 0.3 μM, v_{max} = 0.24 ± 0.01 min^{-1}). As expected from the results in Figure 4C,F, the *para*-NO_2-C9-benzamide aTC analogue (**14**) did not promote NADPH consumption at any concentration tested. Lineweaver–Burke plots for aTC (**1**) against Tet(X7) and Tet(50) suggest mixed competitive inhibition for variable TC. We were unable to obtain Lineweaver–Burke plots for aTC (**1**) with variable NADPH due to the dose-dependent enhancement of NADPH oxidation by aTC and assume this observed activity is due to an uncompetitive binding interaction (Figure 4H). These findings support unique inhibition mechanisms for aTC (**1**) as a competitive slow substrate for type 1 TDases and a mixed competitive inhibitor for type 2 TDases. Lineweaver–Burke plots for *para*-NO_2-C9-benzamide-aTC (**14**) against Tet(50) with variable TC (Figure 5A) and variable NADPH (Figure 5B) support a model for competitive inhibition with respect to both TC and NADPH. The same trend was true, although less pronounced, for compound **14** against Tet(X7) (Figure S15). These

https://doi.org/10.1021/acs.jmedchem.2c01629
J. Med. Chem. 2023, 66, 3917–3933

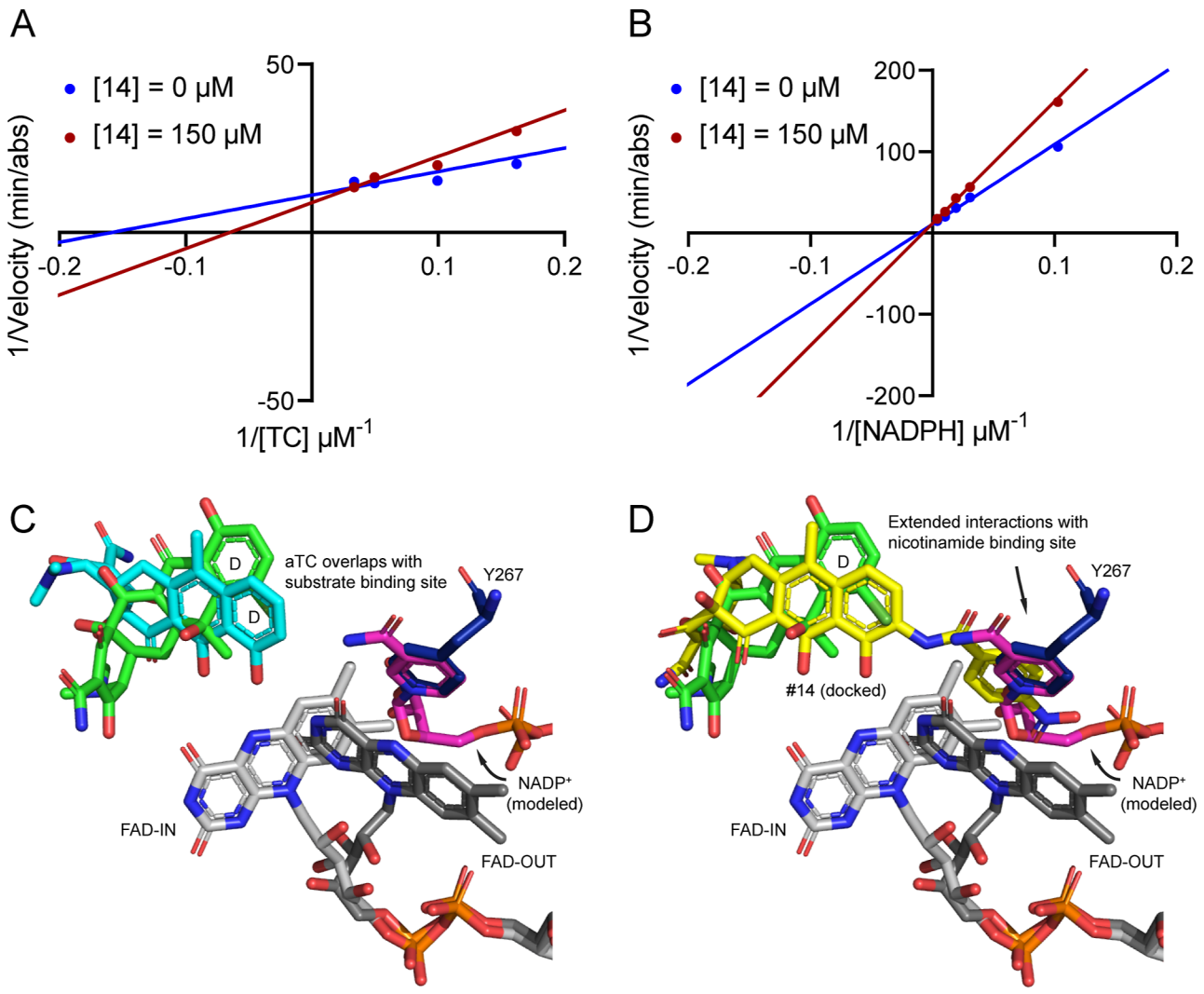

Figure 5. C9-benzamide/benzylamine-aTC analogues are bisubstrate TDase inhibitors. Lineweaver−Burke plots support thecompetitive nature of Tet(50) inhibition by compound **14** with respect to (A) TC and (B) NADPH. (C) Overlay of the liganded X-ray crystal structures of Tet(50) bound to CTC (PDB: 5TUI) and aTC (PDB: 5TUF) highlights the distinct ligand binding modes and conformation of the FAD cofactor (FAD-IN for CTC; FAD-OUT for aTC). $NADP^+$ was manually docked to highlight the presumed overlap of the space occupied by the Y267 sidechain or the $NADP^+$/NADPH nicotinamide ring in stabilizing the FAD-OUT conformation through $\pi-\pi$ stacking with the FAD isoalloxazine ring system. (D) Molecular docking of compound **14** captures the bifunctional binding mode where the aTC core scaffold overlaps with the original aTC binding mode with extended interactions of the C9-benzamide group across a solvent-exposed channel to allow for stabilization of the FAD isoalloxazine ring system through $\pi-\pi$ stacking with overlap of the ligand space previously occupied by the Y267 sidechain or the $NADP^+$/NADPH nicotinamide ring.

findings, along with molecular docking (Figures 1E, 5C,D, and S1), validate the bisubstrate nature of C9-benzamide/benzylamine-aTC analogues as TDase inhibitors.

A variety of TDase inhibitors have been reported, including AZT,[43] bismuth salts,[44] flavonoids,[45] and aTC.[16] The development of selective inhibitors for enzymes in the FMO superfamily has been challenging due in part to the mechanistic complexity, dynamic nature, and substrate flexibility observed for this enzyme class.[46] aTC represents a cell permeable privileged scaffold from which to build better TDase inhibitors. Bisubstrate FMO inhibitors are promising given that the potential to inhibit multiple steps of the catalytic cycle and to enhance binding affinity through extended ligand engagement across multiple binding sites.[47] Bisubstrate inhibitors spanning the TC and NADPH binding sites of TDases are conceptually possible given these two ligands seem to have unique and adjacent binding sites near the dynamic FAD cofactor in class A FMOs.[35,48] The NADPH binding site in class A FMOs has not been fully elucidated; however, the co-crystal structure of a mutant version of *para*-hydroxybenzoate hydroxylase (PHBH) complexed to NADPH suggests that the NADPH binding site is located on a surface-exposed groove between the substrate and FAD-binding domains.[49] The crystallographically observed NADPH binding mode in PHBH appears to have the nicotinamide extended away from the active site, although molecular modeling by the GSK group with KMO supports an alternate binding mode that better supports a functional model for reduction of FAD adopting the solvent-exposed "OUT" conformation.[35,36] Hence, bisubstrate inhibitors could in principle be constructed via fusion of the substrate and nicotinamide scaffolds (Figure 5C,D). This concept has been demonstrated against the enzyme KMO and is validated in this work for TDases.[35]

https://doi.org/10.1021/acs.jmedchem.2c01629
J. Med. Chem. 2023, 66, 3917−3933

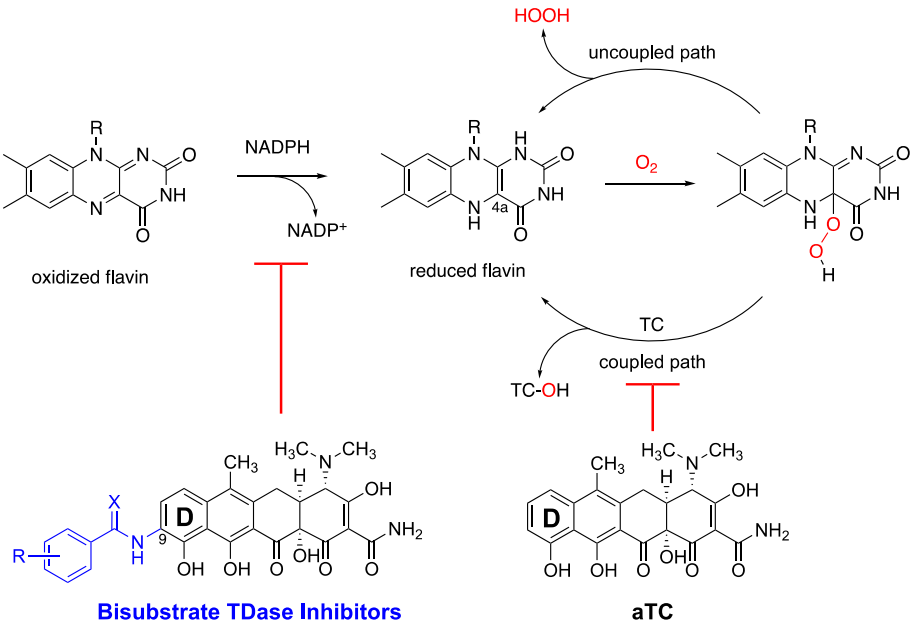

Figure 6. Bisubstrate TDase inhibitors block reduction of FAD by competitively binding to the TC and NADPH sites to prevent the formation of the peroxy flavin intermediate. aTC blocks the oxidation of TC and promotes the uncoupled formation of hydrogen peroxide by competitively binding to the TC site. aTC can be turned over as a competitive sacrificial substrate for type 1 TDases.

Our findings validate the promise of non-antibacterial TDase inhibitors to overcome TC resistance caused by enzymatic inactivation. Through the development of bisubstrate TDase inhibitors, we have engineered out the inherent antibacterial activity of the parent aTC scaffold and improved selectivity and potency for TDase inhibition. We predict that this will widen the therapeutic window of TDase inhibitors and eliminate the potential for the TDase inhibitor to serve as a selection factor for resistance. aTC (**1**) acts as a competitive sacrificial substrate for type 1 TDases [Tet(X7)] and a mixed competitive inhibitor for type 2 TDases [Tet(50)]. This suggests that aTC potentially samples multiple binding modes in the TDase active sites—TC substrate-like binding mode with FAD-"IN" for type 1 TDases and aTC inhibitor binding mode with FAD-"OUT" for type 2 TDases. The bisubstrate inhibitor **14** was competitive with both TC and NADPH for both type 1 [Tet(X7)] and type 2 [Tet(50)] TDases and was not turned over as a substrate by either enzyme type. This is consistent with our working model for bisubstrate inhibition, where the C9-substituted aTC analogues bind in the TC site via the core aTC scaffold and the NADPH nicotinamide site via $\pi-\pi$ stacking of the C9-benzamide/benzylamine aryl group with the isoalloxazine heterocycle of FAD in the "OUT" conformation (Figure 5D). Bisubstrate TDase inhibitors act upstream of the parent aTC inhibitor scaffold by inhibiting the reduction of FAD to $FADH_2$, which is a prerequisite for the formation of a reactive C4a-peroxy-flavin intermediate. This could explain why bisubstrate TDase inhibitors are not substrates for type 1 TDases. The bisubstrate nature might also stabilize the inhibitor binding mode preventing sampling of the substrate binding mode that might explain turnover of aTC as a slow substrate by type 1 TDases. aTC stimulates NADPH oxidation and FAD reduction, leading to a futile cycle of the "uncoupled" oxidative path, resulting in the accumulation of H_2O_2 (Figure 6).

There is no deposited structure of a type 1 TDase with the FAD cofactor in the "OUT" conformation, which limited our ability to pursue rigorous molecular docking to the type 1 enzymes without a validated structural model. It is presumed that FAD dynamics are conserved across type 1 and type 2 enzymes, but it is noteworthy that type 1 enzymes lack the conserved Y267 found to stabilize FAD in the "OUT" conformation in type 2 enzymes. However, the overall loop architecture is conserved across type 1 and type 2 enzymes, with a Leu residue at the analogous 267 position in type 1 enzymes. The inability of Leu267 to stabilize FAD in the "OUT" conformation might be limiting the ability to capture this conformation in structural studies due to an increase in flavin and protein dynamics. Bisubstrate TDase inhibitors slow or block NADPH oxidation and FAD reduction for both type 1 and type 2 TDases (Figure 4), further supporting a shared model of bisubstrate TDase inhibition through competitive binding at the substrate and nicotinamide sites. Hence, we propose that the binding mode of bisubstrate TDase inhibitors can be controlled by extended interactions between aryl substitutions and the FAD isoalloxazine heterocycle in both type 1 and type 2 enzymes (Figure 5D).

The SAR explored in this study revealed that the C9-benzamides are more potent than the C9-benzylamines and that *para*-substitution of the phenyl ring with an electron-withdrawing group (NO_2 or CF_3) was preferred. The more rigid amide linkage might better align the benzamide to facially interact with the FAD isoalloxazine. However, the water solubility of the C9-benzylamines was significantly better than that of the C9-benzamides, which is critical for preclinical advancement. Hence, we propose that benzylic substitution of the C9-benzylamine series might help to rigidify the inhibitor to bias the binding conformation while preserving the water solubility and adding beneficial metabolic stability (given benzylic positions are often the site of oxidation via general metabolism).[50] The modest whole cell activity of the bisubstrate inhibitors might also be associated to reduced cell permeability relative to aTC, leading to low cell accumulation in *E. coli*.[51] Despite the advancements made in

https://doi.org/10.1021/acs.jmedchem.2c01629
J. Med. Chem. 2023, 66, 3917−3933

this study, the bisubstrate TDase inhibitors require further optimization of solubility, potency, stability, selectivity, and cellular accumulation. This could potentially be achieved through systematic exploration of the C9-aryl substituent to leverage existing knowledge of favorable aromatic heterocycle $\pi-\pi$ stacking interactions.[52] These bisubstrate compounds present a new mechanism of TDase inhibition with the opportunity for further rational design to improve effectiveness of overcoming TDase resistance when used in combination with TC antibiotics.

CONCLUSIONS

We synthesized and characterized bisubstrate inhibitors of TDase resistance enzymes via scaffold fusion of a known inhibitor, aTC (**1**), and benzamide/benzylamine structural mimics of nicotinamide (Figure 5). Inhibitor design was guided by molecular modeling using the co-crystal structure of aTC and the type 1 TDase Tet(50). Modeling identified the C9-position of the aTC D-ring as the ideal attachment point for aryl nicotinamide isosteres to promote $\pi-\pi$ stacking with the FAD isoalloxazine heterocycle in the solvent-exposed "OUT" conformation to simulate the structural environment of the reductive step of the catalytic cycle. We validated the bisubstrate nature of the C9-functionalized TDase inhibitors against type 1 [Tet(X7)] and type 2 [Tet(50)] TDase enzymes and established important SARs via in vitro biochemical characterization. aTC (**1**) is a competitive inhibitor with respect to TC and is uncompetitive with respect to NADPH. aTC is a competitive sacrificial substrate against type 1 TDases and promotes the uncoupled reduction of FAD by NADPH. However, *para*-NO_2-C9-benzamide aTC inhibitor **14** is competitive with both TC and NADPH and blocks reduction of FAD by NADPH. This compound is stable toward type 1 and type 2 TDases, consistent with a bisubstrate mode of TDase inhibition where the FAD "OUT" conformation is stabilized by the inhibitor binding mode. aTC (**1**) rescues TC activity against resistant *E. coli* strains expressing TDases and also exhibits inherent antibacterial activity. Bisubstrate TDase inhibitors are non-antibacterial agents capable of rescuing TC antibacterial activity against *E. coli* expressing type 1 or type 2 TDases. Hence, TDase inhibition via combination therapy is a viable therapeutic approach for overcoming TC resistance via enzymatic inactivation.

EXPERIMENTAL SECTION

General Materials and Methods. All in vitro kinetic assays and whole cell bacterial growth assays were prepared open to air in non-degassed buffer solutions using sterile technique. All organic solvents, including deuterated NMR solvents and reagent chemicals used in the preparation or analysis of synthetic compounds, were obtained commercially and used without further purification. TC (HCl salt), NADPH (tetrasodium salt), and G6P dehydrogenase *Leuconostoc mesenteroides* [recombinant, expressed in *E. coli*, suspension in $(NH_4)_2SO_4$] were purchased from Millipore-Sigma (St. Louis, MO). aTC (HCl salt) was purchased from Chemodex (United Kingdom). $NADP^+$ (hydrate) was purchased from Carbosynth (Compton, England). G6P was purchased from Chem-Impex (Wood Dale, IL). NMR spectra were obtained on a Varian Unity-Inova 500 MHz or Agilent Premium Compact+ 600 MHz spectrometer in 5 mm type 1, class A borosilicate glass NMR tubes (Wilman LabGlass part no. 535-PP-8). All free induction decay files were processed using Mestrenova version 11.0.4 software. Chemical shifts (δ) are reported in parts per million (ppm) and referenced to residual non-deuterated solvent. Coupling constants (J) are reported in hertz (Hz). TDase in vitro reactions were monitored by optical absorbance spectroscopy on an Agilent Cary 50 UV−visible spectrophotometer using polystyrene cuvettes and LC−MS using an Agilent 6130 single quadrupole instrument (ESI+) with G1313 autosampler, G1315 diode array detector, and 1200 series solvent module with separation on a Phenomenex Gemini C18 column, 50 × 2 mm (5 μm) fit with a guard column cassette. LC−MS solvents were 0.1% formic acid in H_2O (A) and 0.1% formic acid in ACN (B). Solvent gradient was linear, starting from 0% B to 95% B over 20 min at a flow rate of 0.5 mL/min. HPLC was performed on an HP1050 system using a Luna 10 mm C18(2) 100 Å column (250 mm × 21.2 mm) from Phenomenex fitted with a guard column of the same matrix (15 mm × 21.2 mm). HPLC solvents were 0.1% formic acid in H_2O (A) and 0.1% formic acid in ACN (B), with a gradient formed from 0% B to 95% B over 20 min at a flow rate of 9 mL/min. LC−MS and HPLC data were processed using ChemStation software version B.04.02 SP1. Liquid medium bacterial growth assays were performed using Difco BBL Mueller−Hinton broth in Costar 96-well plates at 37 °C. End-point growth density was judged by OD_{600} measurement using a Synergy H1 plate reader (BioTek, Inc.). Solid medium bacterial growth assays were performed using Mueller−Hinton no. 2 (MHII) agar, and inhibition zone sizes were measured using a Neiko electronic caliper. SDS-PAGE analysis was carried out using Bio-Rad Any kD precast polyacrylamide gels with staining by Coomassie brilliant blue and comparison to a Bio-Rad Precision Plus Protein Dual Xtra pre-stained protein standard ladder.

Compound Purity Statement. All compounds are >95% pure by HPLC analysis. Epimerization of some compounds, presumably at C4, was observed. The "epimeric purity" of each test compound was determined by LCMS and is reported in the Experimental Section.

Synthesis of C9-Substituted aTC Derivatives. *C9−NO-aTC (**2**).* A 25 mL Erlenmeyer flask was charged with aTC (0.1814 g, 0.392 mmol) and 9 mL of 0.1 M HCl (aq) and cooled to 0 °C in an ice water bath to form a bright yellow suspension. Solid $NaNO_2$ (0.0406 g, 0.588 mmol) was dissolved in 2.2 mL of 0.1 M HCl (aq) in a separate vial and was transferred dropwise over 15 min to the suspension of aTC at 0 °C. The rusty orange reaction mixture was then filtered through a 0.45 μm PTFE syringe filter into a 100 mL round bottom flask containing 10 mL of MeOH to give a dark red filtrate. The original reaction flask was washed with 3 × 5 mL of 0.1 M HCl (aq), and the washes were subsequently filtered through the same syringe filter into the 100 mL round bottom flask. The solution was concentrated under reduced pressure via rotary evaporation to yield a reddish-orange residue. The residue was dissolved in minimal amounts of MeOH and diluted with 150 mL of Et_2O and cooled to 4 °C to induce precipitation of the product. After ∼24 h, the solvent was removed via pipet, and the orange solid was triturated with fresh Et_2O. The solid was dried under a stream of N_2 gas to yield compound **2** as the corresponding HCl salt (powdery, bright orange solid; 0.1659 g, 86% yield). The resulting solid was used for the next step without further purification. ^{1}H NMR (500 MHz, DMSO-d_6): δ (ppm) 9.29 (s, 1H) 6.66−6.59 (m, 2H), 3.22 (d, J = 17 Hz, 1H), 3.00 (dd, J = 17 Hz, 5 Hz), 2.39 (s, 6H), 2.22 (s, 3H). ^{13}C NMR (151 MHz, DMSO-d_6): δ (ppm) 192.4, 167.0, 141.5, 118.8, 117.7, 42.0, 40.3, 26.5, 13.6. LCMS purity 98%. MS (ESI+): $[M + H]^+$; found, 455.9. High-resolution mass spectrometry (HRMS) (time-of-flight (TOF) MS ESI+): calcd for $C_{22}H_{21}N_3O_8$ $[M + H]^+$, 456.1401; found, 456.1387.

*C9−NH$_2$-aTC (**3**).* Compound **2** (0.1659 g, 0.337 mmol) was added as a solid to an oven-dried 100 mL round-bottom flask. The solid was dissolved in a few mL of MeOH, and 25 drops of 1 M NaOH (aq) were added while gently swirling the flask. The resulting dark reddish-purple solution was concentrated under reduced pressure via rotary evaporation and dried for ∼48 h under vacuum to yield a dark purple solid. After drying under vacuum, the flask was backfilled with Ar gas and charged with 17 mL of anhydrous MeOH (DriSolv). The flask was sonicated to help dissolve residual solids. The flask was charged with 10% Pd/C (0.008 g, 5% by mass) and exposed to H_2 gas with direct bubbling into the MeOH solution (15 min). After 15 min, the vent needle was removed, and the reaction mixture was left to stir

https://doi.org/10.1021/acs.jmedchem.2c01629
J. Med. Chem. 2023, 66, 3917−3933

under an H_2 atmosphere (~1 atm balloon) until complete (5 h as judged by LC−MS analysis). The reaction mixture was acidified by the addition of 8 mL of 1 M HCl (aq) prior to filtration through Celite. The filtrate and combined MeOH washings were concentrated under reduced pressure via rotary evaporation to yield a brown residue. The residue was dissolved in a minimal amount of MeOH, diluted with 150 mL Et_2O, and cooled to 4 °C to induce precipitation of the product. After ~24 h, the solvent was removed via pipet, and the light brown solid was triturated with fresh Et_2O. The solid was dried under a stream of N_2 gas to yield compound **3** as the corresponding HCl salt (powdery, light brown solid; 0.1264 g, 73% yield). The resulting solid was used for the next step without further purification. ^{1}H NMR (600 MHz, DMSO-d_6): δ (ppm) 9.60 (s, 1H), 9.23 (s, 1H), 7.63−7.51 (m, 1H), 7.44 (d, J = 8.1 Hz, 1H), 7.38 (d, J = 6.7 Hz, 1H), 3.49−3.45 (m, 3H), 2.97−2.91 (m), 2.38 (s, 3H). ^{13}C NMR (151 MHz, DMSO-d_6): δ (ppm) 188.1, 172.6, 172.1, 121.7, 115.2, 112.4, 108.9, 97.8, 97.1, 76.8, 76.3, 66.7, 66.2, 44.3, 34.0, 26.3, 15.2, 14.0. LCMS purity 99%. MS (ESI+): $[M + H]^+$; found, 442.0. High-resolution mass spectrometry (HRMS) (time-of-flight (TOF) MS ESI+): calcd for $C_{22}H_{23}N_3O_7$ $[M + H]^+$, 442.1609; found, 442.1594.

General Procedure (A) for the Synthesis of C9-Amido-aTC Analogues (4−15). Acetic acid (0.056 mL, 0.972 mmol) and DIPEA (0.271 mL, 1.556 mmol) were dissolved in 26 mL of anhydrous DMF (DriSolv) in a dry 100 mL round-bottom flask charged with HATU (0.3696 g, 0.972 mmol). The clear solution turned pale yellow and was stirred at room temperature for 10 min before the addition of compound **3** (HCl salt). The dark brown reaction solution was stirred for 5 min at room temperature, and then quenched with 5 mL of 1 M HCl (aq) and concentrated under reduced pressure via rotary evaporation to yield a dark brown residue. The residue was dissolved in MeOH, filtered through a 0.45 μm PTFE syringe filter, and purified by RP-C18 prep-HPLC to provide the desired products **4−15** as the corresponding formic acid salts.

*(4S,4aS,12aS)-9-Acetamido-4-(dimethylamino)-3,10,11,12a-tetrahydroxy-6-methyl-1,12-dioxo-1,4,4a,5,12,12a-hexahydrotetracene-2-carboxamide (**4**).* Compound **4** was prepared according to general procedure A and was obtained in 25% yield as a brown solid. ^{1}H NMR (500 MHz, DMSO-d_6): δ 9.64 (d, J = 4.2 Hz, 0H), 9.34 (s, 1H), 9.23 (s, 2H), 9.14 (s, 2H), 8.96 (s, 1H), 8.12 (t, J = 10 Hz, 2H), 7.37 (d, J = 8.8 Hz, 1H), 7.08 (s, 1H), 6.81 (s, 1H), 4.66 (s, 1H), 3.16−3.09 (m, 2H), 2.93 (s, 4H), 2.42 (s, 6H), 2.36 (s, 3H), 2.22 (s, 2H), 2.11 (d, J = 7.8 Hz, 4H). ^{13}C NMR (126 MHz, DMSO-d_6): δ 168.6, 164.6, 163.0, 135.2, 41.7, 38.3, 23.8, 23.6, 13.9, 13.7. Prep-HPLC t_R 13m. LCMS epimeric purity 82%. MS (ESI+): $[M + H]^+$; found, 483.8. High-resolution mass spectrometry (HRMS) (time-of-flight (TOF) MS ESI+): calcd for $C_{24}H_{25}N3O_8$ $[M + H]^+$, 484.1714; found, 484.1697.

*(4S,4aS,12aS)-9-(5-Aminopentanamido)-4-(dimethylamino)-3,10,11,12a-tetrahydroxy-6-methyl-1,12-dioxo-1,4,4a,5,12,12a-hexahydrotetracene-2-carboxamide (**5**).* Compound **5** was prepared according to general procedure A and was obtained in 21% yield as a brown solid. ^{1}H NMR (500 MHz, DMSO-d_6): δ 8.76 (d, J = 4.4 Hz, 1H), 8.52 (d, J = 8.4 Hz, 1H), 7.95 (s, 1H), 7.52 (d, J = 4.4 Hz, 1H), 7.50 (d, J = 4.4 Hz, 1H), 3.16 (s, 3H), 3.13−3.10 (m, 2H), 2.89 (s, 6H), 2.73 (s, 5H), 2.43 (s, 1H), 2.16−2.11 (m, 2H), 2.07 (s, 1H) 1.69−1.65 (m, 2H), 1.65−1.59 (m, 2H). ^{13}C NMR (126 MHz, DMSO-d_6): δ 172.60, 172.08, 170.44, 162.30, 161.68, 159.39, 151.07, 149.08, 139.66, 136.39, 134.60, 128.80, 120.87, 120.68, 116.23, 112.27, 109.31, 109.19, 97.12, 77.03, 76.35, 53.26, 48.58, 41.25, 38.25, 35.79, 34.06, 31.17, 30.77, 21.89, 20.55, 16.70, 14.08, 14.02, 1.16. Prep-HPLC t_R 13m. LCMS epimeric purity 60%. MS (ESI+): $[M + H]^+$; found, 540.3. High-resolution mass spectrometry (HRMS) (time-of-flight (TOF) MS ESI+): calcd for $C_{27}H_{32}N_4O_8$ $[M + H]^+$, 540.2215; found, 540.2452.

*(4S,4aS,12aS)-9-Benzamido-4-(dimethylamino)-3,10,11,12a-tetrahydroxy-6-methyl-1,12-dioxo-1,4,4a,5,12,12a-hexahydrotetracene-2-carboxamide (**6**).* Compound **6** was prepared according to general procedure A and was obtained in 21% yield as a brown solid. ^{1}H NMR (500 MHz, DMSO-d_6): δ (ppm) 8.08−8.02 (m, 3H), 7.64−7.53 (m, 4H) 3.16 (s, 3H), 2.98−2.94 (m, 1H), 2.90−2.88 (m, 1H), 2.44 (s, 1H), 2.40 (s, 1H), 2.07 (s, 6H). ^{13}C NMR (125 MHz, DMSO-d_6): δ (ppm) 165.2, 136.0, 134.2, 131.7, 130.2, 128.5, 128.2, 127.6, 126.9, 121.3, 118.0, 114.9, 112.1, 108.9, 76.4, 48.5, 47.9, 47.7, 47.6, 47.4, 47.2. Prep-HPLC t_R 14m. LCMS epimeric purity 98%. MS (ESI+): calcd for $C_{29}H_{27}N_3O_8$ $[M + H]^+$, 546.2; found, 546.2.

*(4S,4aS,12aS)-9-(2-Nitrobenzamido)-4-(dimethylamino)-3,10,11,12a-tetrahydroxy-6-methyl-1,12-dioxo-1,4,4a,5,12,12a-hexahydrotetracene-2-carboxamide (**7**).* Compound **7** was prepared according to general procedure A and was obtained in 5% yield as an orange solid. ^{1}H NMR (500 MHz, DMSO-d_6): δ (ppm) 8.19 (d, J = 9 Hz, 1H), 8.15 (d, J = 9 Hz, 1H), 7.88 (t, J = 7.5 Hz, 1H), 7.79 (d, J = 8 Hz, 1H), 7.75 (d, J = 8 Hz, 1H), 7.62−7.56 (m, J = 5 Hz, 1H), 3.54−3.42 (m, 1H), 3.01 (s, 1H), 2.98−2.94 (m, 1H), 2.89 (s, 6H), 2.44 (s, 3H). ^{13}C NMR (125 MHz, DMSO-d_6): δ (ppm) 172.6, 172.1, 164.7, 162.9, 148.6, 146.5, 134.0, 132.6, 130.8, 129.3, 124.1, 121.2, 114.9, 112.1, 76.9, 76.4, 48.6, 35.8, 14.0. Prep-HPLC t_R 14m. LCMS epimeric purity 75%. MS (ESI+): $[M + H]^+$; found, 591.2. High-resolution mass spectrometry (HRMS) (time-of-flight (TOF) MS ESI+): calcd for $C_{29}H_{26}N_4O_{10}$ $[M + H]^+$, 591.1722; found, 591.1720.

*(4S,4aS,12aS)-9-(2-Fluorobenzamido)-4-(dimethylamino)-3,10,11,12a-tetrahydroxy-6-methyl-1,12-dioxo-1,4,4a,5,12,12a-hexahydrotetracene-2-carboxamide (**8**).* Compound **8** was prepared according to general procedure A and was obtained in 8% yield as a dark orange solid. ^{1}H NMR (500 MHz, DMSO-d_6): δ 9.71 (d, J = 7.6 Hz, 2H), 8.42 (d, J = 8.9 Hz), 7.91 (t, J = 7.2 Hz, 2H), 7.87 (td, J = 7.9, 1.6 Hz, 1H), 7.67−7.62 (m, 3H), 7.58 (d, J = 8.9 Hz), 7.41 (d, J = 9.6 Hz, 2H), 7.38 (d, J = 7.2 Hz, 2H), 7.32 (td, J = 4.5, 1.2 Hz, 1H), 7.30 (d, J = 7.9 Hz, 1H), 3.17 (s, 6H), 2.43 (s, 3H). ^{13}C NMR (125 MHz, DMSO-d_6): δ (ppm) 134.7, 134.6, 131.9, 130.8, 124.9, 124.5, 124.4, 117.0, 116.8, 116.3, 112.0, 76.4, 64.9, 48.6. Prep-HPLC t_R 14m. LCMS epimeric purity 95%. MS (ESI+): $[M + H]^+$; found, 564.2. High-resolution mass spectrometry (HRMS) (time-of-flight (TOF) MS ESI+): calcd for $C_{29}H_{26}FN_3O_8$ $[M + H]^+$, 564.1777; found, 564.1775.

*(4S,4aS,12aS)-9-(2-Chlorobenzamido)-4-(dimethylamino)-3,10,11,12a-tetrahydroxy-6-methyl-1,12-dioxo-1,4,4a,5,12,12a-hexahydrotetracene-2-carboxamide (**9**).* Compound **9** was prepared according to general procedure A and was obtained in 10% yield as an orange solid. ^{1}H NMR (500 MHz, DMSO-d_6): δ (ppm) 8.17 (d, J = 8.9, 1H) 7.67−7.63 (m, 1H), 7.60−7.57 (m, 1H), 7.57−7.55 (s, 1H), 7.55−7.50 (m, 1H), 7.50−7.45, (m, 1H), 3.55−3.50 (m, 1H), 3.16 (s, 3H), 2.99−2.95 (m, 1H), 2.89 (s, 1H), 2.47−2.42 (m, 1H), 2.36 (s, 6H). ^{13}C NMR (125 MHz, DMSO-d_6): δ (ppm) 165.3, 136.4, 131.2, 130.1, 129.7, 129.3, 127.2, 115.0, 48.6, 30.7, 14.0. Prep-HPLC t_R 14m. LCMS epimeric purity 75%. MS (ESI+): $[M + H]^+$; found, 579.6. High-resolution mass spectrometry (HRMS) (time-of-flight (TOF) MS ESI+): calcd for $C_{29}H_{26}ClN_3O_8$ $[M + H]^+$, 580.1481; found, 580.1465.

*(4S,4aS,12aS)-9-(2-Iodobenzamido)-4-(dimethylamino)-3,10,11,12a-tetrahydroxy-6-methyl-1,12-dioxo-1,4,4a,5,12,12a-hexahydrotetracene-2-carboxamide (**10**).* Compound **10** was prepared according to general procedure A and was obtained in 16% yield as a brown solid. ^{1}H NMR (500 MHz, DMSO-d_6): δ 8.16 (d, J = 9 Hz, 1H), 7.94 (d, J = 7.7, 1H), 7.59−7.50 (m, 3H), 7.24 (td, J = 7.7, 2.0, 1H), 3.52−3.48 (m, 1H), 3.03−3.01 (m, 1H), 2.98−2.94 (m, 2H), 2.44 (s, 1H), 2.39 (s, 3H). ^{13}C NMR (125 MHz, DMSO-d_6): δ (ppm) 172.6, 167.9, 163.0, 142.5, 139.1, 131.1, 128.2, 128.0, 112.2, 93.8, 76.4, 64.9, 15.2, 14.0. LCMS epimeric purity 97%. MS (ESI+): M + $H]^+$; found, 671.6. High-resolution mass spectrometry (HRMS) (time-of-flight (TOF) MS ESI+): calcd for $C_{29}H_{26}IN_3O_8$ $[M + H]^+$, 672.0837; found, 672.0819.

*(4S,4aS,12aS)-9-(3-Fluorobenzamido)-4-(dimethylamino)-3,10,11,12a-tetrahydroxy-6-methyl-1,12-dioxo-1,4,4a,5,12,12a-hexahydrotetracene-2-carboxamide (**11**).* Compound **11** was prepared according to general procedure A and was obtained in 6% yield as an orange solid. ^{1}H NMR (500 MHz, DMSO-d_6): δ 8.03−7.75 (m), 7.60−7.57 (m), 7.44−7.41 (m), 7.35−7.30 (m), 3.17 (s), 2.89 (s), 2.73 (s), 2.43−2.32 (m). Prep-HPLC t_R 14m. LCMS epimeric purity 98%. MS (ESI+): $[M + H]^+$; found, 564.2. High-

https://doi.org/10.1021/acs.jmedchem.2c01629
J. Med. Chem. 2023, 66, 3917−3933

resolution mass spectrometry (HRMS) (time-of-flight (TOF) MS ESI +): calcd for $C_{29}H_{26}FN_3O_8$ $[M + H]^+$, 564.1777; found, 564.1761.

*(4S,4aS,12aS)-9-(3-Chlorobenzamido)-4-(dimethylamino)-3,10,11,12a-tetrahydroxy-6-methyl-1,12-dioxo-1,4,4a,5,12,12a-hexahydrotetracene-2-carboxamide (**12**).* Compound **12** was prepared according to general procedure A and was obtained in 5% yield as an orange solid. ^{1}H NMR (500 MHz, DMSO-d_6): δ 10.00 (s, 1H), 9.64 (s, 1H), 9.38 (d, J = 13.4 Hz, 1H), 9.24 (s, 2H), 8.09−8.07 (m, 1H), 7.99−7.96 (m, 3H), 7.69 (ddd, J = 8.0, 2.1, 0.9 Hz, 2H), 7.61−7.53 (m, 3H), 3.39−3.36 (m), 3.17 (s, 1H), 2.91 (s, 6H), 2.44 (s, 3H), 2.41−2.39 (m, 1H). ^{13}C NMR (125 MHz, DMSO-d_6) 172.1, 168.6, 163.0, 150.0, 136.8, 136.3, 133.3, 131.5, 130.5, 130.3, 127.5, 127.4, 126.4, 121.0, 114.9, 112.3, 108.9, 76.34, 14.00, 13.60. Prep-HPLC t_R 14m. LCMS epimeric purity 98%. MS (ESI+): $[M + H]^+$; found, 580.2. High-resolution mass spectrometry (HRMS) (time-of-flight (TOF) MS ESI+): calcd for $C_{29}H_{26}ClN_3O_8$ $[M + H]^+$, 580.1481; found, 580.1467.

*(4S,4aS,12aS)-9-(4-Bromobenzamido)-4-(dimethylamino)-3,10,11,12a-tetrahydroxy-6-methyl-1,12-dioxo-1,4,4a,5,12,12a-hexahydrotetracene-2-carboxamide (**13**).* Compound **13** was prepared according to general procedure A and was obtained in 5% yield as a dark brown solid. ^{1}H NMR (500 MHz, DMSO-d_6): δ 9.92 (d, J = 6.2 Hz, 1H), 7.98 (t, J = 8.0 Hz, 4H), 7.76 (d, J = 8.5 Hz, 2H), 7.54 (dd, J = 9.1, 5.8 Hz, 2H), 4.94 (d, J = 3.0 Hz, 1H), 2.87 (s, 1H), 2.77 (d, J = 4.6 Hz, 1H), 2.43 (s, 6H), 2.39 (s, 3H). Prep-HPLC t_R 14m. LCMS epimeric purity 65%. MS (ESI+): $[M + H]^+$; found, 623.5. High-resolution mass spectrometry (HRMS) (time-of-flight (TOF) MS ESI+): calcd for $C_{29}H_{26}BrN_3O_8$ $[M + H]^+$, 624.0976; found, 624.0962.

*(4S,4aS,12aS)-9-(4-Nitrobenzamido)-4-(dimethylamino)-3,10,11,12a-tetrahydroxy-6-methyl-1,12-dioxo-1,4,4a,5,12,12a-hexahydrotetracene-2-carboxamide (**14**).* Compound **14** was prepared according to general procedure A and was obtained in 15% yield as a rusty orange solid. ^{1}H NMR (600 MHz, DMSO-d_6): δ 8.38 (d, J = 7.5, 2H), 8.25 (d, J = 7.5, 2H), 7.99 (d, J = 9, 1H), 7.57−7.54 (m, 1H), 3.50−3.44 (m, 1H), 3.17−3.07 (m, 1H), 3.00−2.97 (m, 1H), 2.86−2.81 (m, 1H), 2.54 (s, 6H) ^{13}C NMR (151 MHz, DMSO-d_6): δ 199.19, 190.07, 187.99, 172.58, 172.21, 163.88, 163.22, 162.35, 150.16, 149.22, 148.87, 140.51, 140.01, 136.49, 134.15, 131.88, 130.73, 130.59, 130.40, 129.22, 128.82, 123.62, 123.44, 122.14, 121.93, 120.73, 120.68, 118.58, 114.84, 114.65, 112.26, 112.21, 108.93, 97.06, 76.86, 76.39, 67.10, 66.25, 44.49, 40.43, 38.43, 27.16, 26.08, 14.04, 14.00. Prep-HPLC t_R 14m. LCMS epimeric purity 90%. MS (ESI+): $[M + H]^+$; found, 590.6. High-resolution mass spectrometry (HRMS) (time-of-flight (TOF) MS ESI+): calcd for $C_{29}H_{26}N_4O_{10}$ $[M + H]^+$, 591.1722; found, 591.1708.

*(4S,4aS,12aS)-4-(Dimethylamino)-3,10,11,12a-tetrahydroxy-6-methyl-1,12-dioxo-9-(2-phenylacetamido)-1,4,4a,5,12,12a-hexahydrotetracene-2-carboxamide (**15**).* Compound **15** was prepared according to general procedure **A** and was obtained in 30% yield as a brown oil. ^{1}H NMR (600 MHz, DMSO-d_6): δ 8.08 (d, 1H), 7.38−7.23 (m, 7H), 3.56 (s, 2H), 2.99−2.94 (m, 2H) 2.61 (s, 2H), 2.37 (s, 6H), 2.32−2.24 (m, 2H), 2.18 (s, 3H). Prep-HPLC t_R 16m. LCMS epimeric purity 95%. MS (ESI+): calcd for $C_{30}H_{29}N_2O_8$ $[M + H]^+$, 559.2; found, 559.9.

General Procedure (B) for Synthesis of C9-Amino-aTC Analogues (16−20). To a clean, dry round-bottom flask, equipped with a stir bar, was added C9−NH_2-aTC-NH_2 HCl salt (compound **3**) (0.1069 mmol) as a solution in 5.0 mL of anhydrous MeOH (DriSolv) under an Ar atmosphere. A solution of Et_3N (14.91 mL, 0.1069 mmol) in 1.5 mL of anhydrous MeOH was prepared in a separate vial and transferred to the brown stirring solution of **3**. The benzaldehyde substrate (0.1925 mmol) was dissolved in 1 mL of anhydrous MeOH in a separate vial and transferred to the reaction in one portion. $Na(OAc)_3BH$ (0.0793 g, 0.3742 mmol) was added in one portion to the reaction mixture as a solid. The reaction mixture was stirred for 3 h at room temperature prior to the addition of a second portion of $Na(OAc)_3BH$ (0.0226 g, 0.1069 mmol). The reaction mixture was stirred for an additional 3 h prior to quenching with a solution of saturated $NaHCO_3$ (aq). The quenched reaction mixture was concentrated under reduced pressure via rotary evaporation. The dark red solid was dissolved in MeOH and filtered through a 0.45 μM PTFE syringe filter prior to purification by RP-C18 prep-HPLC to provide the desired products **16−20** as the corresponding formic acid salts.

*(4S,4aS,12aS)-9-Benzylamino-4-(dimethylamino)-3,10,11,12a-tetrahydroxy-6-methyl-1,12-dioxo-1,4,4a,5,12,12a-hexahydrotetracene-2-carboxamide (**16**).* Compound **16** was prepared according to general procedure B and was obtained in 22% yield as a red solid. ^{1}H NMR (600 MHz, DMSO-d_6): δ (ppm) 7.36 (d, J = 7.5 Hz, 1H), 7.30 (d, J = 7.4 Hz, 2H), 7.28 (d, 1H), 7.20 (d, J = 7.4 Hz, 2H), 6.93−6.89 (m, 1H), 3.28−3.23 (m, 1H), 3.05−2.99 (m, 1H), 2.63−2.59 (m, 1H), 2.53 (s, 3H), 2.41 (s, 6H), 2.26 (d, 1H) ^{13}C NMR (151 MHz, DMSO-d_6): δ 193.25, 192.62, 191.41, 173.03, 163.04, 157.84, 157.05, 141.57, 134.59, 132.87, 129.84, 129.49, 129.25, 129.17, 128.83, 128.65, 128.57, 128.47, 128.21, 126.89, 126.84, 126.36, 126.30, 117.40, 116.23, 113.53, 113.22, 112.01, 111.85, 109.73, 46.76, 42.36, 41.73, 34.39, 32.41, 31.10, 29.02, 24.59, 22.64, 22.03, 17.02, 13.99, 13.59. Prep-HPLC t_R 16m. LCMS epimeric purity 92%. MS (ESI+): $[M + H]^+$; found, 531.8. High-resolution mass spectrometry (HRMS) (time-of-flight (TOF) MS ESI+): calcd for $C_{29}H_{29}N_3O_7$ $[M + H]^+$, 532.2078; found, 532.2079.

*(4S,4aS,12aS)-9-(4-Nitrobenzylamino)-4-(dimethylamino)-3,10,11,12a-tetrahydroxy-6-methyl-1,12-dioxo-1,4,4a,5,12,12a-hexahydrotetracene-2-carboxamide (**17**).* Compound **17** was prepared according to general procedure B and was obtained in 5% yield as a red solid. ^{1}H NMR (600 MHz, DMSO-d_6): δ 8.27 (d, J = 8.7 Hz, 1H), 8.20 (d, J = 8.7 Hz, 2H), 8.14 (s, 1H), 7.59 (d, J = 8.6 Hz, 2H), 5.53 (t, J = 5.5 Hz, 1H), 4.64 (d, J = 5.1 Hz, 2H), 3.30 (s, 20H), 2.62−2.60 (m, 1H), 2.48−2.45 (m, 3H), 2.40 (s, 3H), 2.36 (s, 13H). ^{13}C NMR (151 MHz, DMSO-d_6): δ 163.06, 137.82, 130.65, 128.17, 127.70, 127.03, 124.30, 123.91, 123.62, 123.29, 61.99, 41.81, 29.02, 13.71. Prep-HPLC t_R 16m. LCMS epimeric purity 90%. MS (ESI+): calcd for $C_{29}H_{28}N_4O_9$ $[M + H]^+$, 577.2; found, 576.7.

*(4S,4aS,12aS)-9-(4-Methylbenzylamino)-4-(dimethylamino)-3,10,11,12a-tetrahydroxy-6-methyl-1,12-dioxo-1,4,4a,5,12,12a-hexahydrotetracene-2-carboxamide (**18**).* Compound **18** was prepared according to general procedure B and was obtained in 20% yield as a red solid. ^{1}H NMR (600 MHz, DMSO-d_6): δ (ppm) 7.83 (d, J = 7.9 Hz, 1H), 7.30 (d, J = 7.9 Hz, 1H), 7.24 (d, J = 7.4 Hz, 2H), 7.09 (d, J = 7.4 Hz, 2H), 4.41 (s, 2H), 3.28−3.25 (m, 1H), 3.05−3.02 (m, 1H), 2.63−2.60 (m, 1H), 2.39−2.37 (m, 1H) 2.38 (s, 6H), 2.37 (s, 3H), 2.24 (s, 3H). ^{13}C NMR (151 MHz, DMSO-d_6): δ (ppm) 191.55, 177.41, 173.03, 172.76, 167.28, 163.03, 157.73, 143.01, 137.58, 137.21, 135.58, 135.32, 132.81, 130.88, 129.83, 129.31, 129.21, 129.10, 128.87, 128.60, 128.00, 127.14, 126.92, 126.83, 125.44, 117.65, 116.24, 115.25, 113.39, 113.18, 111.73, 109.71, 108.01, 76.59, 47.14, 46.70, 45.70, 41.73, 40.29, 34.36, 26.99, 24.58, 23.90, 21.11, 20.63, 13.71, 13.56. Prep-HPLC t_R 16m. LCMS epimeric purity 98%. MS (ESI+): $[M + H]^+$, 545.8. High-resolution mass spectrometry (HRMS) (time-of-flight (TOF) MS ESI+): calcd for $C_{30}H_{31}N_3O_7$ $[M + H]^+$, 546.2235; found, 546.2235.

*(4S,4aS,12aS)-9-(4-Bromobenzylamino)-4-(dimethylamino)-3,10,11,12a-tetrahydroxy-6-methyl-1,12-dioxo-1,4,4a,5,12,12a-hexahydrotetracene-2-carboxamide (**19**).* Compound **19** was prepared according to general procedure B and was obtained in 30% yield as a bright red solid. ^{1}H NMR (600 MHz, DMSO-d_6): δ (ppm) 7.86 (d, J = 8.3 Hz, 1H), 7.70 (d, J = 8.3, 1H), 7.51 (d, J = 8.1 Hz, 2H), 7.27 (d, J = 8.1 Hz, 2H), 4.46 (s, 2H), 3.32 (s, 6H), 3.25−3.15 (m, 1H), 3.02−2.94 (m, 1H), 2.38 (s, 3H), 2.25−2.23 (m, 1H) ^{13}C NMR (151 MHz, DMSO-d_6): δ (ppm) 163.02, 141.91, 140.48, 131.55, 131.20, 130.80, 128.46, 119.42, 62.03, 41.79, 28.92, 24.51. Prep-HPLC t_R 16m. LCMS epimeric purity 98%. MS (ESI+): $[M + H]^+$, 609.9. High-resolution mass spectrometry (HRMS) (FT-ICR APCI$^+$) calcd for $C_{29}H_{28}BrN_3O_7$ $[M + H]^+$, 610.1183; found, 610.1163.

*(4S,4aS,12aS)-9-(4-Trifluoromethylbenzylamino)-4-(dimethylamino)-3,10,11,12a-tetrahydroxy-6-methyl-1,12-dioxo-1,4,4a,5,12,12a-hexahydrotetracene-2-carboxamide (**20**).* Compound **20** was prepared according to general procedure B and was obtained in 25% yield as a red solid. ^{1}H NMR (600 MHz, DMSO-d_6): δ (ppm) 7.66 (d, J = 8.1 Hz, 2H), 7.57 (d, J = 8.1 Hz, 2H), 7.25 (d, J

https://doi.org/10.1021/acs.jmedchem.2c01629
J. Med. Chem. 2023, 66, 3917−3933

= 8.9 Hz, 1H), 7.00 (d, J = 8.9 Hz, 1H), 4.57 (s, 2H), 3.27 (d, J = 16 Hz, 2H), 3.09−3.02 (m, J = 17, 16, 5.9 Hz, 1H), 2.54 (s, 1H), 2.38 (s, 5H), 2.27 (s, 3H). ^{13}C NMR (151 MHz, DMSO-d_6): δ (ppm) 172.76, 163.02, 146.19, 145.69, 132.53, 130.09, 129.61, 129.32, 128.53, 127.55, 127.35, 127.14, 126.93, 125.52, 125.15, 123.45, 121.65, 117.29, 111.59, 108.04, 76.54, 45.74, 41.69, 39.92, 39.78, 39.64, 39.50, 39.36, 39.22, 39.08, 34.36, 28.99, 23.89, 13.70, 13.54, 8.59. Prep-HPLC t_R 16m. LCMS epimeric purity 99%. MS (ESI+): calcd for $C_{30}H_{28}F_3N_3O_7$ $[M + H]^+$, 600.2; found, 600.2.

*(4S,4aS,12aS)-9-Phenethylamino-4-(dimethylamino)-3,10,11,12a-tetrahydroxy-6-methyl-1,12-dioxo-1,4,4a,5,12,12a-hexahydrotetracene-2-carboxamide (**21**).* To a clean, dry round-bottom flask, equipped with a stir bar, was added aTC-NH_2 hydrochloride (compound **3**) (63.8 mg, 0.124 mmol) and DriSolv methanol (6.0 mL) under an argon atmosphere. Et_3N (18.7 μL, 0.1341 mmol) was dissolved in 1.2 mL of methanol in a separate vial and transferred to the brown stirring solution. The dark red reaction mixture was cooled to 0 °C. Phenylacetaldehyde, synthesized via Dess−Martin oxidation of phenethyl alcohol, was dissolved in 1 mL of methanol in a separate vial and transferred to the reaction. The reaction was stirred for 5 min. $Na(OAc)_3BH$ (0.0788 g, 0.3720 mmol) was added in one portion, and the reaction was stirred for 1 h. The reaction was quenched with a saturated sodium bicarbonate solution and concentrated under reduced pressure. The dark red solid was filtered through a 0.45 μM PTFE syringe filter and purified by preparative HPLC (t_R = 15m) to provide the formate salt (pink solid, 0.0110 g, 15% yield). ^{1}H NMR (600 MHz, DMSO-d_6): δ (ppm) 7.34−7.23 (m, 10H), 3.56 (s, 2H), 3.21−3.18 (m, 2H), 3.10−3.06 (m, 1H), 2.94−2.90 (m, 1H), 2.73−7.69 (m, 1H), 2.39 (s, 8H) ^{13}C NMR (151 MHz, DMSO): δ 172.66, 139.62, 135.00, 129.34, 128.72, 128.65, 128.37, 128.33, 128.21, 126.81, 126.55, 126.08, 108.05, 47.83, 45.71, 44.68, 40.67, 39.94, 39.80, 39.66, 39.52, 39.38, 39.24, 39.10, 35.10, 34.37, 31.69, 13.78. LCMS epimeric purity 90%. MS (ESI+): $[M + H]^+$, 546.0. High-resolution mass spectrometry (HRMS) (time-of-flight (TOF) MS ESI+) calcd for $C_{30}H_{31}N_3O_7$ $[M + H]^+$, 546.2235; found, 546.2242.

Cloning, Expression, and Purification of TDases. All genes encoding TDases used in this study were cloned into pET28b(+) vectors (Novagen) as previously described (BamHI and NdeI restriction sites) and transformed into BL21-Star (DE3) competent cells (Life Technologies). Cells were cultured at 37 °C in lysogeny broth (LB) containing kanamycin (Kan) at 0.03 mg/mL (final concentration); once the culture reached an OD_{600} of ∼0.6, the cells were cooled to 0 °C in an ice water bath. Protein expression was induced by the addition of 1 mM IPTG (final concentration), and cells were grown at 15 °C for 12−15 h. To harvest protein, the induced cells were pelleted by centrifugation at 4000 rpm for 15 min (4 °C) and resuspended in cold 40 mL of lysis buffer (50 mM K_2HPO_4, 500 mM NaCl, 20 mM imidazole, 10% glycerol, 5 mM BME, pH 8.0) containing SIGMAFAST protease inhibitor (Millipore-Sigma). Cell suspensions were flash frozen in liquid nitrogen and stored at −80 °C. Frozen cell suspensions were thawed and mechanically lysed using an Avestin EmulsiFlex-C5 cell disruptor, and the resultant lysate was clarified via ultracentrifugation at 45,000 rpm for 35 min at 4 °C. The clarified supernatant was transferred to a fritted column containing washed and equilibrated Ni-NTA resin and incubated for 30−45 min with gentle rocking. Resin was then washed with lysis buffer (2 × 40 mL), and the protein was eluted from the resin with elution buffer (5 × 10 mL elutions, 50 mM K_2HPO_4, 500 mM NaCl, 5 mM BME, 300 mM imidazole, 10% glycerol, pH 8.0). Fractions containing the desired proteins (as judged by SDS-PAGE analysis) were combined and transferred to a 10,000 molecular weight cutoff (MWCO) Snakeskin dialysis tubing (Thermo Scientific) and equilibrated in dialysis buffer (50 mM K_2HPO_4 pH 8.0, 150 mM NaCl, 1 mM DTT) overnight. Dialyzed protein solutions were concentrated using a 30,000 MWCO Amicon centrifugal filter (Millipore-Sigma), and the concentrated protein solution was flash frozen as beads in liquid nitrogen (50 μL portions) and stored at −80 °C. The % FAD for each batch of protein varies and is determined by back calculation from a denaturated aliquot of enzyme using optical absorbance with the published extinction coefficient of 11,300 M^{-1} cm^{-1} for FAD. On average, batches of Tet(50) and Tet(X7) ranged from 20 to 60% FAD with an average of 30% FAD for batches of Tet(50) and 50% FAD for batches of Tet(X7).

Characterization of Substrate and Inhibitor Degradation and Hydrogen Peroxide Detection by In Vitro TDase Reaction. TDase reactions were prepared in 100 mM TAPS buffer (pH 8.5) with an NADPH regenerating system (40 mM G6P, 4 mM $NADP^+$, 1 mM $MgCl_2$, 4 U/mL G6P dehydrogenase) or 252 μM NADPH and 5.04 mM $MgCl_2$, 20 μM substrate (15 μM substrate and 30 μM inhibitor in mixed assays), and 0.24 μM TDase enzyme [Tet(X7) and Tet(50)] (all concentrations represent final protein concentrations based on absorbance at 280 nm with % FAD-bound protein ranging from 20 to 60% batch-to-batch). Reaction progress was monitored by optical absorbance spectroscopy (280−550 nm, 5 min intervals) over 2 h. Aliquots of reaction sample (150 μL) were removed and quenched (600 μL of 1:1 acetonitrile/0.25 M aqueous HCl) immediately after enzyme was added (0 min) and at 5, 30, 60, 90, and 120 min intervals. The quenched samples were centrifuged (5000 rpm, 4 °C) for 5 min, and 600 μL of the resulting supernatant was mixed with an Fmoc-Ala internal standard (3.12 μM final concentration) and analyzed by LC−MS in positive ion mode (single trial). Extracted ion chromatograms for the expected $[M + H]^+$ molecular ions corresponding to substrate and mono-hydroxylated product were normalized to the Fmoc-Ala internal standard $[M + H]^+$ counts. A separate 20 μL aliquot of the reaction mixture was removed at 0, 5, 30, 60, 90, and 120 min timepoints and used for colorimetric detection of hydrogen peroxide formation performed using an aqueous Pierce Quantitative Peroxide Assay Kit (Thermo Scientific). Each 20 μL aliquot (performed in triplicate on three separate aliquots for each timepoint) was added to a 96-well plate containing 200 μL of working reagent (prepared according to specifications for the Pierce Quantitative Peroxide Assay Kit). The plate was incubated for at least 20 min at room temperature, and optical absorbance was measured at 595 nm. Control reactions containing no TDase enzyme or no compound were also performed to determine background signals, and no significant substrate/inhibitor degradation or H_2O_2 formation were observed (Figure S16).

Apparent Steady-State Kinetics of aTC Inactivation and Inhibitor Acceleration of NADPH Consumption. Reactions were prepared in 100 mM TAPS buffer at pH 8.5 with varying amounts of aTC (0−60 μM), 504 μM NADPH, 5.04 mM $MgCl_2$, and 0.4 μM TDase (final protein concentration; working concentration of the active enzyme is predicted to be 0.08−0.24 μM based on FAD content). Reactions were initiated by the addition of TDase and were monitored continuously via optical absorbance spectroscopy at 440 nm for aTC degradation or 360 nm for NADPH consumption for 2 min (performed in triplicate as independent trials). Initial enzyme velocities were determined by linear regression using Agilent Cary WinUV Software over the linear range of the reaction (typically between 0 and 1 min), plotted against the concentration of the substrate, and fitted to the Michaelis−Menten equation using GraphPad Prism 6.

Lineweaver−Burke Kinetics of Inhibition of NADPH and TC Consumption. Reactions were prepared in 100 mM TAPS buffer at pH 8.5 with varying amounts of NADPH [3−65 μM for Tet(X7); 3−260 μM for Tet(50)] or TC [2−30 μM for both Tet(X7) and Tet(50)], 5.04 mM $MgCl_2$, and 0.4 μM TDase (final protein concentration; working concentration of active enzyme is predicted to be 0.08−0.24 μM based on FAD content). Reactions were initiated by the addition of TDase and were monitored continuously via optical absorbance spectroscopy at 400 nm for up to 2 min (performed in triplicate as independent trials). Initial enzyme velocities were determined by linear regression using Agilent Cary WinUV Software over the linear range of the reaction (typically between 0 and 1 min), plotted against the concentration of the substrate, and fitted to the Michaelis−Menten equation using GraphPad Prism 6.

Determination of Apparent TDase Inhibitor IC_{50} Values. Half-maximal inhibitory concentrations (IC_{50}) for the inhibition of Tet(X7) and Tet(50) were determined from the velocities of TC

https://doi.org/10.1021/acs.jmedchem.2c01629
J. Med. Chem. 2023, 66, 3917−3933

degradation in the presence of varying concentrations of inhibitor. Reaction samples were prepared in 100 mM TAPS buffer (pH 8.5) with 504 μM NADPH, 5.04 mM $MgCl_2$, 25.3 μM TC, varying concentrations of inhibitor (typically 2−262 μM), and 0.4 μM TDase (final protein concentration; working concentration of active enzyme is predicted to be 0.08−0.24 μM based on FAD content). Reactions were initiated by the addition of TDase and were monitored continuously via optical absorbance spectroscopy at 400 nm for 3 min (performed in triplicate as independent trials). Initial enzyme velocities were determined by linear regression using Agilent Cary WinUV Software over the linear range of the reaction (typically between 0 and 1 min). The velocities were plotted against the logarithm of inhibitor concentration, and apparent IC_{50} values were determined using nonlinear regression analysis in GraphPad Prism v6. Each set of experiments included a no-TDase control reaction, which was used as the full enzyme inhibition velocity and assigned to inhibitor concentration of 1×10^{15}, and a no-inhibitor control, which was assigned an inhibitor concentration of 1×10^{-15}. A no-TC control was also performed to search for potentially competitive background signals generated from the enzymatic degradation of the inhibitor itself. For all inhibitor−enzyme combinations, the initial velocities of the no-TC controls were negligible.

Antibiotic Susceptibility Testing—Broth Microdilution Method. Inhibitors were diluted to 20 mg/mL in DMSO, then diluted to 256 μg/mL in cation-adjusted MH-II broth supplemented with 50 μg/mL Kan. Inhibition panels were prepared by performing a two-fold dilution series of each inhibitor, including a no-drug control, resulting in a concentration gradient of 0−128 μg/mL in MH-II broth containing a constant concentration of TC (16 μg/mL; final working concentration). *E. coli* MegaX (Invitrogen) expressing a TDase [Tet(X7) or Tet(50)] in the pZE21 plasmid vector were cultured to an OD_{600} of 0.3−0.8, then inoculated into the inhibition panel for a final concentration of $\sim 5 \times 10^6$ cfu/mL, including three replicates per inhibitor and a no-inocula control column. Plates were sealed with Breathe-Easy membranes (Sigma-Aldrich) and incubated at 37 °C. For end-point growth assays, plates were shaken at 225 rpm, and OD_{600} was measured at 20 h using a Synergy H1 plate reader (BioTek). For growth rate assays, inhibition panels were placed in a BioStack plate stacker (BioTek), and every 10−20 min panels were shaken for 30 s, followed by OD_{600} measured using the Synergy H1 plate reader. The resulting growth curves were log-transformed, and a rolling regression with a shifting window of 1 h was applied, such that the maximum slope of any of the regressions is the exponential growth rate.[53] If one of the three technical replicates showed no growth while the other two had growth (or vice versa), or droplets on the Breathe-Easy membrane were observed, those wells were masked. For each strain-[inhibitor] combination, growth rates were compared to the no-inhibitor control using a one-way ANOVA with p-values corrected for multiple hypotheses using the Benjamini−Hochberg method (FDR) in Prism. The growth rates were plotted against the logarithm of inhibitor concentration, and apparent IC_{50} values were determined using nonlinear regression analysis in GraphPad Prism v6. A control reaction containing only TC in MH-II broth at 37 °C was performed to determine background TC degradation, and no significant non-enzymatic degradation was observed (Figure S17).

Antibiotic Susceptibility Testing—Agar Diffusion Method. Antibacterial activity of the compounds was determined by a modified Kirby−Bauer agar diffusion assay.[54] Overnight cultures of *E. coli* MegaX (Invitrogen) expressing a TDase [Tet(X7) or Tet(50)] from the pZE21 plasmid vector were grown in LB broth containing 4 μg/mL TC and 50 μg/mL Kan for 18−24 h. Standardized cell suspensions of a 0.5 McFarland standard (OD_{600} ~0.08−0.1) were prepared in MH-II broth. Each standardized cell suspension (0.1 mL) was added to 35 mL of sterile, melted MH-II agar containing 4 μg/mL TC and 50 μg/mL Kan tempered to 47−50 °C. After gentle mixing, the inoculated agar media was poured into a sterile plastic Petri dish (145 mm × 20 mm) and allowed to solidify. Wells of 9.0 mm diameter were cut from the Petri dish agar and filled with 50 μL of the test sample solution. Substrate alone wells contained 4 mg/mL TC or 0.5 mg/mL tigecycline. All wells with inhibitor contained 0.25 mg/mL of the corresponding inhibitor, and all wells contained 80% DMSO v/v. Controls for 80% DMSO v/v were performed and resulted in no observable growth inhibition. The Petri dish was incubated at 37 °C for ~24 h, and the inhibition zone diameters were measured (mm) with an electronic caliper.

Bio-layer Interferometry. BLI experiments were performed on an Octet RED384 system (FortéBio) with super streptavidin pins (Sartorius). Tet(50) and Tet(X7) were biotinylated using EZ-Link NHS-PEG4-Biotin No-Weigh Format (Thermo Scientific) and Pierce Biotin Quantitation Kit to quantify biotinylation. Experiments were conducted in a running buffer of HEPES (pH = 7.5) supplemented with 150 mM NaCl, 0.005% tween 20, 1 mM $MgCl_2$, and 5% DMSO. Data were processed using double-reference subtraction with the protein-binding signal corrected by subtracting signal of both immobilized protein into the buffer and biotin-loaded pin into the ligand (Figure S10).

Preparation of Receptors and Ligands for Molecular Docking. All computations were performed using the Schrödinger platform (release 2021-1) accessed through the SBGrid consortium.[55] Ligands and protein were prepared as previously described.[56] In brief, ligands were obtained using 2D sketcher in maestro (version 12.7.156). Different 3D structural and chemical possibilities of ligands were enumerated using LigPrep.[57] Epik was used to generate ionization states at pH 7.0 ± 2.0.[58] The receptor was prepared from chain B of PDB ID 5TUF[59] using the protein preparation wizard.[60] The protein was pre-processed to add hydrogens, to fill in missing sidechains and to delete water molecules. The bound inhibitor, aTC (TDC in PDB ID 5TUF), was deleted. An alternate rotamer was selected for Tyr267 such that the hydroxyphenyl side chain flips away from the FAD-interacting region (Figure S1A). Different tautomeric states of the bound co-factor, FAD, were generated at pH 7.0 ± 2.0, and the conformation with the least clash score was chosen. H-bonds were assigned using PROPKA at pH 7.0, and thus, the prepared protein was restrained minimized.

Generation of Receptor Grid for Molecular Docking. OPLS_2005 forcefield was used to generate the receptor grid.[61] The grid center was manually adjusted to include the entire active site region. The bound cofactor, FAD, was included in the receptor while generating the grid. An inner box of 10 Å × 10 Å × 10 Å and an outer box of 30 Å × 30 Å × 30 Å were set, and the grid center was fixed at Cartesian coordinates of 18.7, 61.7, and 60.0.

Molecular Docking and Analyses. Molecular docking was performed using Glide[62] with the following parameters: precision mode = standard precision; ligand sampling = flexible; added Epik state penalties to the docking scores; no constrains; and perform post-docking minimization. The docking results were visualized using the pose viewer in maestro. PyMOL v2.3.2 was used to generate images. To validate the docking protocol, the co-crystallized ligand, aTC, was extracted from chain B of Tet(50) (PDB ID: 5TUF) and re-docked into the prepared receptor. aTC binds with a docking score of −7.21 kcal/mol, and the docked conformation overlaps with the co-crystallized conformation (Figure S1B). The validated docking protocol was used to predict the binding modes of aTC derivatives (compounds **14** and **20**) in Tet(50) as described in the main text.

■ ASSOCIATED CONTENT

Supporting Information

The Supporting Information is available free of charge at https://pubs.acs.org/doi/10.1021/acs.jmedchem.2c01629.

Receptor preparation and validation of the docking protocol; LCMS analysis of aTC and *epi*-aTC; LCMS analysis of TC and *epi*-TC; *epi*-TC and TC substrate screens for Tet(X7) and Tet(50); *epi*-aTC substrate screens for Tet(X7) and Tet(50); *epi*-aTC inhibitor screens for Tet(X7) and Tet(50); apparent IC_{50} curves for inhibition of Tet(X7) by compounds **1**−**21** with TC as the substrate; apparent IC_{50} curves for inhibition of Tet(50) by compounds **1**−**21** with TC as the substrate;

https://doi.org/10.1021/acs.jmedchem.2c01629
J. Med. Chem. 2023, 66, 3917−3933

apparent IC_{50} curves for inhibition of Tet(X7) by aTC or compound **14** with tigecycline as the substrate; BLI analysis of TC, aTC, and compound **14** binding to Tet(X7) and Tet(50); inhibitor growth rate statistical comparisons; apparent IC_{50} curves for inhibition of *E. coli* growth in the presence of TC in combination with aTC, compound **4**, compound **14**, or compounds **16**−**20** with expression of Tet(50) or Tet(X7); whole cell inhibition of TC antibiotic degradation by aTC, compound **14**, and compound **20**; quantification of H_2O_2 generation from TDase-catalyzed reactions; steady-state kinetic plots for compound **14** in competition with TC and NADPH; control experiments for in vitro TDase enzymatic assays; stability of TC in MHII broth; and NMR spectra and LCMS traces of compounds **2**−**21** (PDF)

Molecular formula strings and biological data (CSV)

Docked14-in-receptor (PDB)

Docked20-in-receptor (PDB)

AUTHOR INFORMATION

Corresponding Authors

Niraj H. Tolia − *Laboratory of Malaria Immunology and Vaccinology, National Institute of Allergy and Infectious Diseases, National Institute of Health, Bethesda, Maryland 20814, United States;* orcid.org/0000-0002-2689-1337; Phone: 301-761-7537; Email: niraj.tolia@nih.gov

Gautam Dantas − *The Edison Family Center for Genome Sciences and Systems Biology, Washington University School of Medicine, St. Louis, Missouri 63108, United States; Department of Pathology and Immunology, Washington University School of Medicine, St. Louis, Missouri 63110, United States; Department of Molecular Microbiology, Washington University School of Medicine, St. Louis, Missouri 63110, United States; Department of Biomedical Engineering, Washington University in St. Louis, St. Louis, Missouri 63130, United States;* orcid.org/0000-0003-0455-8370; Phone: 314-362-7238; Email: dantas@wustl.edu; Fax: 314-3622156

Timothy A. Wencewicz − *Department of Chemistry, Washington University in St. Louis, St. Louis, Missouri 63130, United States;* orcid.org/0000-0002-5839-6672; Phone: 314-935-7247; Email: wencewicz@wustl.edu; Fax: 314-935-4481

Authors

Emily E. Williford − *Department of Chemistry, Washington University in St. Louis, St. Louis, Missouri 63130, United States*

Caitlin M. DeAngelo − *Department of Chemistry, Washington University in St. Louis, St. Louis, Missouri 63130, United States;* orcid.org/0000-0003-3482-6479

Kevin S. Blake − *The Edison Family Center for Genome Sciences and Systems Biology, Washington University School of Medicine, St. Louis, Missouri 63108, United States*

Hirdesh Kumar − *Laboratory of Malaria Immunology and Vaccinology, National Institute of Allergy and Infectious Diseases, National Institute of Health, Bethesda, Maryland 20814, United States*

Kendrick K. Lam − *Department of Chemistry, Washington University in St. Louis, St. Louis, Missouri 63130, United States*

Katherine V. Jones − *Department of Chemistry, Washington University in St. Louis, St. Louis, Missouri 63130, United States*

Complete contact information is available at: https://pubs.acs.org/10.1021/acs.jmedchem.2c01629

Author Contributions

E.E.W., C. M.D., T.A.W., G.D., and N.H.T. conceived and designed the experiments in this study. E.E.W. and C.M.D. synthesized all TDase inhibitors. E.E.W. and C.M.D. performed all in vitro TDase assays. K.S.B. performed all whole cell studies. H.K. performed the molecular modeling. K.K.L and K.V.J. assisted with synthesis and in vitro TDase assays. E.E.W. and T.A.W. wrote the manuscript, created figures, and compiled the Supporting Information documents with input and approval from all authors.

Funding

This work is supported in part by the National Institute of Allergy and Infectious Diseases (NIAID) of the National Institutes of Health (NIH) through grant 2U01AI123394 awarded to G.D. and T.A.W at Washington University in St. Louis. N.H.T. is supported by the Intramural Research Program of the NIAID of the NIH. K.S.B. is supported by the National Institute of Diabetes and Digestive and Kidney Diseases (T32-DK007130; PI: N. Davidson). E.E.W. is supported by the National Science Foundation through Graduate Research Fellowship (DGE-2139839). The content is solely the responsibility of the authors and does not necessarily represent the official views of the funding agencies.

Notes

The authors declare no competing financial interest.

ACKNOWLEDGMENTS

We thank Drs. Jeff Kao and Manmilan Singh for assistance with multi-dimensional NMR studies in the Department of Chemistry at Washington University in St. Louis. We thank Dr. Henry Rohrs (WashU Chemistry) for assistance with high-resolution mass spectrometry. We thank Dr. Thomas J. Brett for assistance with BLI in the Department of Biochemistry and Molecular Biophysics at Washington University School of Medicine.

ABBREVIATIONS

aTC, anhydrotetracycline; AZT, azidothymidine; DMF, dimethylformamide; DMSO, dimethylsulfoxide; BME, β-mercaptoethanol; FAD, flavin adenine dinucleotide oxidized form; $FADH_2$, flavin adenine dinucleotide reduced form; FMO, flavin monooxygenase; HATU, hexafluorophosphate azabenzotriazole tetramethyl uronium; KMO, kynurenine-3-monooxygenase; MeOH, methanol; NADPH, nicotinamide adenine dinucleotide phosphate reduced form; $NADP^+$, nicotinamide adenine dinucleotide phosphate oxidized form; PHBH, *para*-hydroxybenzoate hydroxylase; TAPS, [tris-(hydroxymethyl)methylamino]propanesulfonic acid; TC, tetracycline; TDase, tetracycline destructase

REFERENCES

(1) Paine, T. F.; Collins, H. S.; Finland, M. Bacteriologic Studies on Aureomycin. *J. Bacteriol.* **1948**, *56*, 489−497.

(2) Nelson, M. L.; Levy, S. B. The history of the tetracyclines. *Ann. N.Y. Acad. Sci.* **2011**, *1241*, 17−32.

(3) Bahrami, F.; Morris, D. L.; Pourgholami, M. H. Tetracyclines: Drugs with Huge Therapeutic Potential. *Mini Rev. Med. Chem.* **2012**, *12*, 44−52.
(4) Griffin, M. O.; Fricovsky, E.; Ceballos, G.; Villarreal, F. Tetracyclines: a pleitropic family of compounds with promising therapeutic properties. Review of the literature. *Am. J. Physiol. Cell Physiol.* **2010**, *299*, C539−C548.
(5) Thaker, M.; Spanogiannopoulos, P.; Wright, G. D. The tetracycline resistome. *Cell. Mol. Life Sci.* **2010**, *67*, 419−431.
(6) Kasbekar, N. T. Tigecycline: A new glycylcycline antimicrobial agent. *Am. J. Health-Syst. Pharm.* **2006**, *63*, 1235−1243.
(7) Zhanel, G. G.; et al. Review of Eravacycline, a novel fluorocycline antibacterial agent. *Drugs* **2016**, *76*, 567−588.
(8) Zhanel, G. G.; et al. Omadacycline: A Novel Oral and Intravenous Aminomethylcycline Antibiotic Agent. *Drugs* **2020**, *80*, 285−313.
(9) Moore, I. F.; Hughes, D. W.; Wright, G. D. Tigecycline is modified by the flavin-dependent monooxygenase TetX. *Biochemistry* **2005**, *44*, 11829−11835.
(10) Gasparrini, A. J.; et al. Tetracycline-inactivating enzymes from environmental, human commensal, and pathogenic bacteria cause broad-spectrum tetracycline resistance. *Commun. Biol.* **2020**, *3*, 241.
(11) Forsberg, K. J.; Patel, S.; Wencewicz, T. A.; Dantas, G. The tetracycline destructases: a novel family of tetracycline-inactivating enzymes. *Chem. Biol.* **2015**, *22*, 888−897.
(12) Yang, W.; et al. TetX is a flavin-dependent monooxygenase conferring resistance to tetracycline antibiotics. *J. Biol. Chem.* **2004**, *279*, 52346−52352.
(13) van Berkel, W. J. H.; Kamerbeek, N. M.; Fraaije, M. W. Flavoprotein monooxygenases, a diverse class of oxidative biocatalysts. *J. Biotechnol.* **2006**, *124*, 670−689.
(14) Volkers, G.; et al. Putative dioxygen-binding sites and recognition of tigecycline and minocycline in the tetracycline-degrading monooxygenase TetX. *Acta Crystallogr., Sect. D: Biol. Crystallogr.* **2013**, *69*, 1758−1767.
(15) Schnappinger, D.; Hillen, W. Tetracyclines: antibiotic action, uptake, and resistance mechanisms. *Arch. Microbiol.* **1996**, *165*, 359−369.
(16) Park, J.; et al. Plasticity, dynamics, and inhibition of emerging tetracycline resistance enzymes. *Nat. Chem. Biol.* **2017**, *13*, 730−736.
(17) Cheng, Q.; et al. Structural and mechanistic basis of the high catalytic activity of monooxygenase Tet(X4) on tigecycline. *BMC Biol.* **2021**, *19*, 262.
(18) Volkers, G.; Palm, G. J.; Weiss, M. S.; Wright, G. D.; Hinrichs, W. Structural basis for a new tetracycline resistance mechanism relying on the TetX monooxygenase. *FEBS Lett.* **2011**, *585*, 1061−1066.
(19) Wright, G. D. Bacterial resistance to antibiotics: enzymatic degradation and modification. *Adv. Drug Deliv. Rev.* **2005**, *57*, 1451−1470.
(20) Pawlowski, A. C.; et al. The evolution of substrate discrimination in macrolide antibiotic resistance enzymes. *Nat. Commun.* **2018**, *9*, 112.
(21) Bush, K.; Jacoby, G. A. Updated Functional Classification of β-Lactamases. *Antimicrob. Agents Chemother.* **2010**, *54*, 969−976.
(22) Kong, K. F.; Schneper, L.; Mathee, K. Beta-lactam antibiotics: from antibiosis to resistance and bacteriology. *APMIS* **2010**, *118*, 1−36.
(23) Aminov, R. I. Evolution in action: dissemination of tet(X) into pathogenic microbiota. *Front. Microbiol.* **2013**, *4*, 192.
(24) He, T.; et al. Emergence of plasmid-mediated high-level tigecycline resistance genes in animals and humans. *Nat. Microbiol.* **2019**, *4*, 1450−1456.
(25) Sun, J.; et al. Plasmid-encoded tet(X) genes that confer high-level tigecycline resistance in Escherichia coli. *Nat. Microbiol.* **2019**, *4*, 1457−1464.
(26) Rudra, P.; Hurst-Hess, K.; Lappierre, P.; Ghosha, P. High levels of intrinsic tetracycline resistance in *Mycobacterium abscessus* are conferred by a tetracycline-modifying monooxygenase. *Antimicrob. Agents Chemother.* **2018**, *62*, No. e00119-18.
(27) Rasmussen, B.; et al. Molecular basis of tetracycline action: identification of analogs whose primary target is not the bacterial ribosome. *Antimicrob. Agents Chemother.* **1991**, *35*, 2306−2311.
(28) Oliva, B.; Gordon, G.; McNicholas, P.; Ellestad, G.; Chopra, I. Evidence that tetracycline analogs whose primary target is not the bacterial ribosome cause lysis of *Escherichia coli*. *Antimicrob. Agents Chemother.* **1992**, *36*, 913−919.
(29) Markley, J. L.; et al. Semisynthetic analogues of anhydrotetracycline as inhibitors of tetracycline destructase enzymes. *ACS Infect. Dis.* **2019**, *5*, 618−633.
(30) Manenda, M. S.; et al. Structural analyses of the Group A flavin-dependent monooxygenase PieE reveal a sliding FAD cofactor conformation bridging OUT and IN conformations. *J. Biol. Chem.* **2020**, *295*, 4709−4722.
(31) Lindqvist, Y.; et al. Structural basis for substrate recognition and specificity in aklavinone-11-hydroxylase from rhodomycin biosynthesis. *J. Mol. Biol.* **2009**, *393*, 966−977.
(32) Ryan, K. S.; et al. Crystallographic trapping in the rebeccamycin biosynthetic enzyme RebC. *Proc. Natl. Acad. Sci. U.S.A.* **2007**, *104*, 15311−15316.
(33) Greenhagen, B. T.; et al. Crystal Structure of the Pyocyanin Biosynthetic Protein PhzS. *Biochemistry* **2008**, *47*, 5281−5289.
(34) Kanteev, M.; et al. A crystal structure of 2-hydroxybiphenyl 3-monooxygenase with bound substrate provides insights into the enzymatic mechanism. *Biochim. Biophys. Acta, Proteins Proteomics* **2015**, *1854*, 1906−1913.
(35) Hutchinson, J. P.; et al. Structural and mechanistic basis of differentiated inhibitors of the acute pancreatitis target kynurenine-3-monooxygenase. *Nat. Commun.* **2017**, *8*, 15827.
(36) Ridder, L.; Mulholland, A. J.; Rietjens, I. M. C. M.; Vervoort, J. A quantum mechanical/molecular mechanical study of the hydroxylation of phenol and halogenated derivatives by phenol hydroxylase. *J. Am. Chem. Soc.* **2000**, *122*, 8728−8738.
(37) Morin, A.; et al. Collaboration gets the most out of software. *Elife* **2013**, *2*, No. e01456.
(38) Remmers, E. G.; Sieger, G. M.; Doerschuk, A. P. Some Observations on the Kinetics of the C•4 Epimerization of Tetracycline. *J. Pharm. Sci.* **1963**, *52*, 752−756.
(39) Degenkolb, J.; Takahashi, M.; Ellestad, G. A.; Hillen, W. Structural requirements of tetracycline-Tet repressor interaction: determination of equilibrium binding constants for tetracycline analogs with the Tet repressor. *Antimicrob. Agents Chemother.* **1991**, *35*, 1591−1595.
(40) Cui, Z.-H.; et al. Rapid detection of plasmid-mediated high-level tigecycline resistance in *Escherichia coli* and *Acinetobacter* spp. *J. Antimicrob. Chemother.* **2020**, *75*, 1479−1483.
(41) Siddens, L. K.; Krueger, S. K.; Henderson, M. C.; Williams, D. E. Mammalian flavin-containing monooxygenase (FMO) as a source of hydrogen peroxide. *Biochem. Pharmacol.* **2014**, *89*, 141−147.
(42) Jiang, Z. Y.; Hunt, J. v.; Wolff, S. P. Ferrous ion oxidation in the presence of xylenol orange for detection of lipid hydroperoxide in low density lipoprotein. *Anal. Biochem.* **1992**, *202*, 384−389.
(43) Liu, Y.; et al. Anti-HIV agent azidothymidine decreases Tet(X)-mediated bacterial resistance to tigecycline in Escherichia coli. *Commun. Biol.* **2020**, *3*, 162.
(44) Deng, T.; et al. Bismuth drugs reverse Tet(X)-conferred tigecycline resistance in gram-negative bacteria. *Microbiol. Spectr.* **2022**, *10*, No. e01578-21.
(45) Xu, L.; et al. A novel inhibitor of monooxygenase reversed the activity of tetracyclines against tet(X3)/tet(X4)-positive bacteria. *EBioMedicine* **2022**, *78*, 103943.
(46) Walsh, C. T.; Wencewicz, T. A. Flavoenzymes: versatile catalysts in biosynthetic pathways. *Nat. Prod. Rep.* **2013**, *30*, 175−200.
(47) Jencks, W. P. On the attribution and additivity of binding energies. *Proc. Natl. Acad. Sci. U.S.A.* **1981**, *78*, 4046−4050.
(48) Crozier-Reabe, K. R.; Phillips, R. S.; Moran, G. R. Kynurenine 3-Monooxygenase from *Pseudomonas fluorescens*: Substrate-like

https://doi.org/10.1021/acs.jmedchem.2c01629
J. Med. Chem. 2023, 66, 3917−3933

Inhibitors both Stimulate Flavin Reduction and Stabilize the Flavin−Peroxo Intermediate yet Result in the Production of Hydrogen Peroxide. *Biochemistry* **2008**, *47*, 12420−12433.
(49) Wang, J.; et al. Protein and ligand dynamics in 4-hydroxybenzoate hydroxylase. *Proc. Natl. Acad. Sci. U.S.A.* **2002**, *99*, 698.
(50) Meunier, B.; de Visser, S. P.; Shaik, S. Mechanism of oxidation reactions catalyzed by cytochrome p450 enzymes. *Chem. Rev.* **2004**, *104*, 3947−3980.
(51) Richter, M. F.; et al. Predictive compound accumulation rules yield a broad-spectrum antibiotic. *Nature* **2017**, *545*, 299−304.
(52) Bootsma, A. N.; Doney, A. C.; Wheeler, S. E. Predicting the Strength of Stacking Interactions between Heterocycles and Aromatic Amino Acid Side Chains. *J. Am. Chem. Soc.* **2019**, *141*, 11027−11035.
(53) Padfield, D.; Castledine, M.; Buckling, A. Temperature-dependent changes to host-parasite interactions alter the thermal performance of a bacterial host. *ISME J.* **2020**, *14*, 389−398.
(54) Bauer, A.; Kirby, W.; Sherris, J.; Turck, M. Antibiotic Susceptibility Testing by a Standardized Single Disk Method. *Am. J. Clin. Pathol.* **1966**, *45*, 493−496.
(55) Morin, A.; et al. Collaboration gets the most out of software. *Elife* **2013**, *2*, No. e01456.
(56) Kumar, H.; Shah, A.; Sobhia, M. E. Novel insights into the structural requirements for the design of selective and specific aldose reductase inhibitors. *J. Mol. Model.* **2012**, *18*, 1791−1799.
(57) Greenwood, J. R.; Calkins, D.; Sullivan, A. P.; Shelley, J. C. Towards the comprehensive, rapid, and accurate prediction of the favorable tautomeric states of drug-like molecules in aqueous solution. *J. Comput. Aided Mol. Des.* **2010**, *24*, 591−604.
(58) Shelley, J. C.; et al. Epik: a software program for pK a prediction and protonation state generation for drug-like molecules. *J. Comput. Aided Mol. Des.* **2007**, *21*, 681−691.
(59) Berman, H. M.; et al. The Protein Data Bank. *Nucleic Acids Res.* **2000**, *28*, 235−242.
(60) Madhavi Sastry, G.; Adzhigirey, M.; Day, T.; Annabhimoju, R.; Sherman, W. Protein and ligand preparation: parameters, protocols, and influence on virtual screening enrichments. *J. Comput. Aided Mol. Des.* **2013**, *27*, 221−234.
(61) Banks, J. L.; et al. Integrated Modeling Program, Applied Chemical Theory (IMPACT). *J. Comput. Chem.* **2005**, *26*, 1752−1780.
(62) Friesner, R. A.; et al. Glide: a new approach for rapid, accurate docking and scoring. 1. method and assessment of docking accuracy. *J. Med. Chem.* **2004**, *47*, 1739−1749.

https://doi.org/10.1021/acs.jmedchem.2c01629
J. Med. Chem. 2023, 66, 3917−3933